

1 **Importance of multiple sources of iron for the upper ocean** 2 **biogeochemistry over the northern Indian Ocean**

3 Priyanka Banerjee¹

4 ¹Divecha Centre for Climate Change, Indian Institute of Science, Bangalore, India.

5 *Correspondence to:* Priyanka Banerjee (pbanerjee@iisc.ac.in)

6

7 **Abstract**

8 Although the northern Indian Ocean (IO) is globally one of the most productive regions and receives dissolved
9 iron (DFe) from multiple sources, there is no comprehensive understanding of how these different sources of DFe
10 can impact upper ocean biogeochemical dynamics. Using an Earth system model with an ocean biogeochemistry
11 component this study shows that atmospheric deposition is the most important source of DFe to the upper 100 m
12 of the northern IO, contributing more than 50% of the annual DFe concentration. Sedimentary sources are locally
13 important in the vicinity of the continental shelves and over the southern tropical IO, away from high atmospheric
14 depositions. While atmospheric depositions contribute to more than 10% (35%) to 0-100 m (surface level)
15 chlorophyll concentrations over large parts of the northern IO, sedimentary sources have similar contribution to
16 chlorophyll concentrations over the southern tropical IO. Such increases in chlorophyll are primarily driven by an
17 increase in diatom population over most of the northern IO. The regions that are susceptible to chlorophyll
18 enhancement following external DFe additions are where low levels of background DFe and high background
19 nitrate-to-iron values are observed. Analysis of DFe budget over selected biophysical regimes over the northern
20 IO points to vertical mixing as the most important mechanism for DFe supply, while the importance of advection
21 (horizontal and vertical) varies seasonally. Apart from removal of surface DFe by phytoplankton uptake,
22 subsurface balance between DFe scavenging and regeneration is crucial in replenishing DFe pool to be made
23 available to surface layer by physical processes.

24 **1 Introduction**

25 Iron is an essential micronutrient for primary producers in the ocean due to the catalytic role of iron in
26 photosynthesis, respiration, and nitrogen fixation (Geider & La Roche, 1994; Raven, 1988). Although iron is one
27 of the most abundant elements in the Earth's crust (McLennan, 2001), its low solubility (Sholkovitz et al., 2012)
28 coupled with an intricate balance between complexation by ligands and high scavenging tendency does not make
29 it readily bioavailable (Boyd & Ellwood, 2010). It has been estimated that iron availability limits primary
30 productivity in as much as ~30% of the global oceans, which results in accumulation of unutilized macronutrients
31 like nitrate and phosphate (Moore et al., 2013a). Even in regions experiencing nitrate limitation of productivity,
32 nitrogen fixation is controlled by the supply of iron (e.g., Mills et al., 2004; Moore et al., 2009; Schlosser et al.,
33 2014). Several artificial iron addition experiments performed in the open oceans have demonstrated its
34 significance in regulating phytoplankton growth (Yoon et al., 2018), while natural iron fertilizations have also
35 shown high levels of carbon export from the upper ocean following increased productivity (e.g., Blain et al., 2007;
36 Pollard et al., 2009).

37 The main external sources of dissolved iron (DFe) to the world oceans are atmospheric depositions (e.g., Conway
38 et al., 2014; Jickells et al., 2005), continental sediments (Elrod et al., 2004; Johnson et al., 1999), river inputs (e.g.,
39 Buck et al., 2007; Canfield, 1997), sea ice (Sedwick & DiTullio, 1997; Wang et al., 2014) and iron seeping from
40 hydrothermal vents (e.g., Nishioka et al., 2013; Tagliabue et al., 2010). Most ocean biogeochemistry models
41 simulating the iron cycle estimate dust ($1.4\text{--}32.7 \text{ Gmol yr}^{-1}$) or sedimentary sources ($0.6\text{--}194 \text{ Gmol yr}^{-1}$) to have
42 the highest contribution to ocean DFe inventory (Tagliabue et al., 2016). However, many of these models do not
43 include hydrothermal sources of DFe. Numerical modelling using dust, sedimentary and hydrothermal sources of
44 DFe have shown that while ocean column DFe inventory is most sensitive to sedimentary and hydrothermal DFe,
45 atmospheric and sedimentary sources of DFe have the largest impact on atmospheric carbon dioxide (Tagliabue
46 et al., 2014). This is because while atmospheric and sedimentary DFe can impact productivity over both the open
47 and coastal oceans, iron from hydrothermal vents reaching the surface water depends on deepwater ventilation
48 and stabilizing impact of organic ligands (Tagliabue et al., 2010; Sander and Koschinsky, 2011). However, with
49 availability of more *in situ* DFe measurements, the relative importance of different sources of DFe are being re-
50 examined at global as well as regional scales.

51 The northern Indian Ocean (IO) is one of the most productive regions of the global oceans, contributing high
52 levels of organic carbon fluxes to the deeper ocean (e.g., Barber et al., 2001; Madhupratap et al., 2003; Rixen et
53 al., 2019). The monsoonal winds drive phytoplankton blooms over different regions of the northern IO, arising
54 from distinct physical mechanisms in different seasons. These mechanisms include blooms due to coastal and
55 open ocean upwelling, advection of nutrients by ocean currents, and mixed layer deepening by winter convection.
56 Episodic blooms are also triggered by passage of cyclones (Kuttippurath et al., 2021) and mesoscale eddies
57 (Prasanna Kumar et al., 2004; Vidya & Prasanna Kumar, 2013). The region hosts one of the most intense oxygen
58 minimum zones of the world oceans (Schmidtko et al., 2017) and is globally one of the major denitrification sites
59 (e.g., Morrison et al., 1999; Bianchi et al., 2012). Several water column measurements have shown that the primary
60 limiting nutrient over the northern IO is reactive nitrogen with possible colimitation by silicate (Košić et al., 2009;
61 Moore et al., 2013a; Morrison et al., 1998). In recent years, a few studies using ocean biogeochemistry models
62 have also pointed to possible iron limitation of phytoplankton blooms during southwest monsoon months (June-
63 September), especially over upwelling regions of the western Arabian Sea (AS), which is the north-western part
64 of the IO (Košić et al., 2009; Wiggert et al., 2007). These findings on the role of iron limitation have also been
65 supported by incubation experiments over the AS during the late southwest monsoon, which have noted
66 chlorophyll enhancements following iron enrichments (Moffett et al., 2015). Furthermore, *in situ* measurements
67 during the late southwest monsoon have revealed complete drawdowns of silicate, owing to its high utilization
68 under iron limitation, as well as high nitrate-to-iron ratios over the western AS (Naqvi et al., 2010). Nutrient
69 enrichment experiments over the central AS during northeast monsoon months (December-March) have also
70 revealed signatures of iron and nitrate colimitation, with addition of these two nutrients supporting increases in
71 diatoms and coccolithophores (Takeda et al., 1995). Colimitation by nitrogen, phosphorus and iron has been
72 identified over the southern Bay of Bengal (BoB, the north-eastern part of the IO) and the eastern equatorial IO
73 (Twining et al., 2019). Thus, availability of iron can have major impacts on availability of other macronutrients
74 and productivity, which can in turn impact denitrification and mid-depth oxygen levels in this region by
75 modulating fluxes of sinking organic matters.

76 In general, there is a reduction in surface DFe concentrations over the northern IO from north to south. Systematic
77 DFe measurements, encompassing all seasons over the AS, conducted during the Joint Global Ocean Flux Study
78 (JGOFS) of the 1990s showed DFe concentrations often exceeding 1 nM, especially during the southwest
79 monsoon (Measures & Vink, 1999). Subsequent measurements revealed lower levels of DFe with surface values
80 ranging between 0.2-1.2 nM over the AS and between 0.2-0.5 nM over the BoB (Chinni et al., 2019; Chinni &
81 Singh, 2022; Grand et al., 2015; Moffett et al., 2015; Vu & Sohrin, 2013). These values are generally higher than
82 most of the open ocean regions. In contrast, southwards of the equatorial IO have surface DFe values generally
83 less than 0.2 nM (e.g., Chinni et al., 2019; Grand et al., 2015; Twining et al 2019; Vu & Sohrin, 2013). The oxygen
84 minimum zone, located to the north of the equator between depths of 150-1000 m, has elevated levels of DFe (>1
85 nM), possibly due to DFe transport from reducing shelf sediments and remineralization of sinking organic matter
86 (Moffett et al., 2007).

87 The overall high values of DFe over the northern IO can stem from multiple external sources of DFe identified
88 within this region: atmospheric aerosol inputs (dust and black carbon) from South and Southwest Asia (Banerjee
89 et al., 2019; Srinivas et al., 2012), continental shelf sediments, high river discharge, especially, over the BoB (e.g.,
90 Chinni et al., 2019; Grand et al., 2015) and hydrothermal vents from the Central Indian Ridge that mainly impact
91 DFe levels at depths of around 3000 m (Nishioka et al., 2013). The importance of episodic dust depositions in
92 alleviating iron limitations of primary productivity over the central AS has been identified, during the northeast
93 monsoon when a deeper ferricline compared to the nitracline yields a high nitrate-to-iron ratio (Banerjee and
94 Kumar, 2014). Additionally, modelling studies over the AS have demonstrated that DFe derived from dust
95 deposition can support about half of the observed primary productivity and a large fraction of nitrogen fixation
96 (Guieu et al., 2019). Centennial-scale model simulations over the IO have revealed that changes in phytoplankton
97 community structure have resulted in increased (reduced) carbon uptake over the eastern (western) IO in response
98 to increased anthropogenic DFe deposition in the present day compared to pre-industrial levels (Pham & Ito,
99 2021). Yet another challenge is that, away from regions with high aerosol loading, other sources of DFe can
100 become important in supporting ocean productivity and controlling patterns of nutrient limitations. Such
101 understanding of relative roles of different sources of DFe in controlling the biogeochemical dynamics of the
102 northern IO remains unexplored. This is important considering the multiple sources of DFe over the northern IO.
103 To this end, the present study uses a suite of simulations from a state-of-the art Earth system model with an iron
104 cycle in its ocean biogeochemistry component to explore the relative contribution of different sources of DFe to
105 phytoplankton blooms and impacts on nutrient availability over the upper 100 m of the northern IO. Furthermore,
106 DFe budget has been analysed over the upper ocean for varied biophysical regimes in this region to identify how
107 different sources of DFe can impact the total DFe budget.

108

109 **2 Data and model**

110 The study uses satellite and reanalysis products, ocean observation data, and an Earth system model to assess
111 contributions of different sources of DFe to phytoplankton blooms over the northern IO. For the present study,
112 the northern IO is considered to encompass 30°N–20°S latitude, 40°–105°E longitude. Thus, the tropical part of
113 the southern IO is also included. Only the open ocean regions, having bottom depth greater than 1000 m, are
114 studied here. The four seasons referred to in this study are defined as: the northeast monsoon: December-March;

115 spring intermonsoon: April-May; southwest monsoon: June-September; and fall intermonsoon: October-
116 November.

117 **2.1 Model**

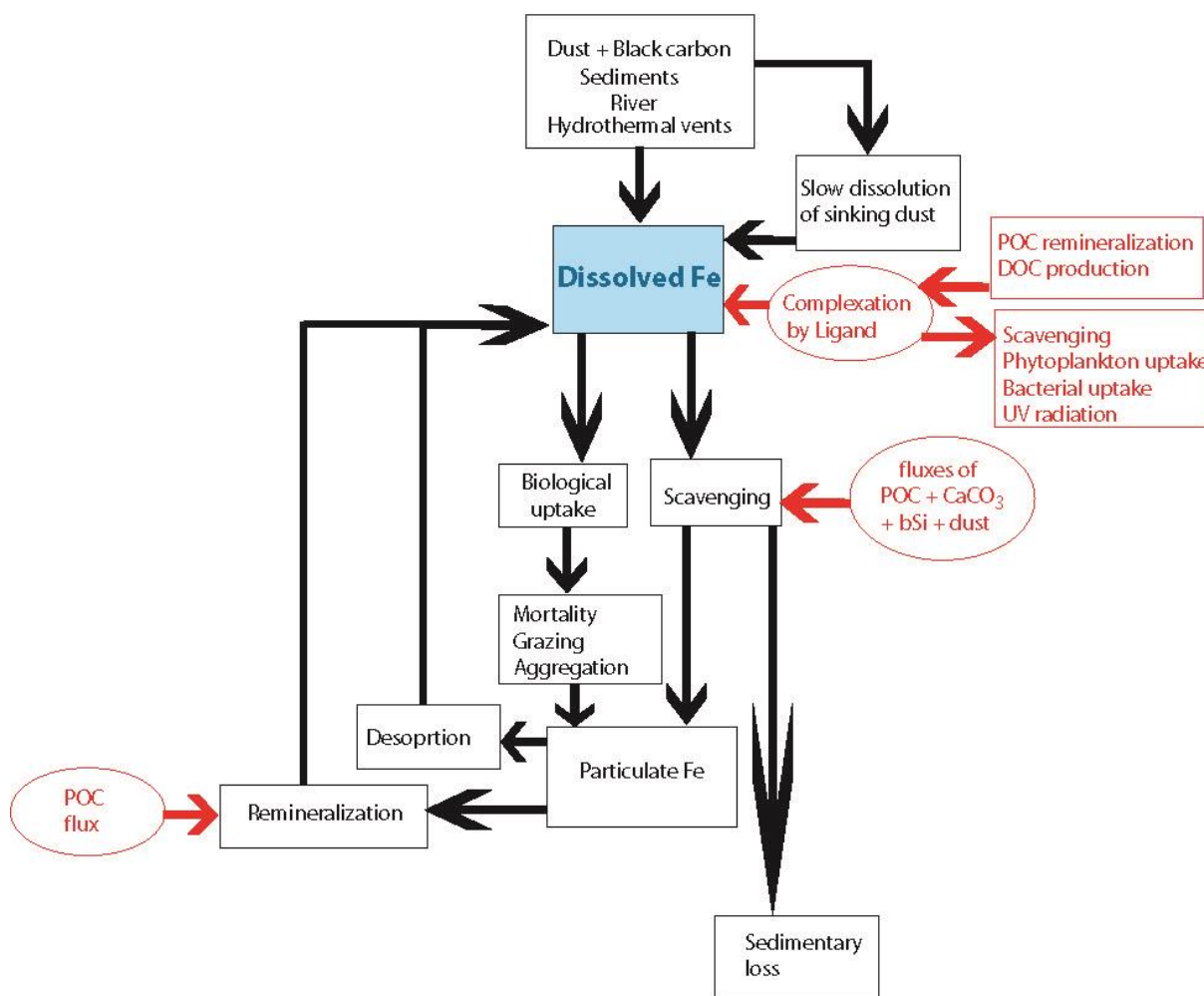
118 This study uses the ocean component Parallel Ocean Program version 2 (POP2) (Smith et al., 2010) embedded in
119 the Community Earth System Model (CESM) version 2.1. This version of CESM incorporates several
120 improvements over previous versions of the model (Danabasoglu et al., 2020). The POP2 model is a level-
121 coordinate model having Arakawa B-grid in the horizontal with North Pole displaced over Greenland. The vertical
122 resolution is 10 m for the upper 160 m and decreases with depth to 250 m in the bottom. The horizontal resolution
123 is nominally 1° with meridional resolution increasing to 0.27° near the equator (Danabasoglu et al., 2012),
124 implying that mesoscale eddies are not resolved. Momentum advection is based on a second-order central
125 advection scheme while tracer advection relies on a third-order upwind advection scheme. Vertical ocean mixing
126 is parameterized using the non-local K-Profile parameterization (Large et al., 1994), which is incorporated into
127 CESM2.1 via the Community Ocean Vertical Mixing (CVMix) framework. Horizontal mixing is parameterized
128 using the Gent and Williams (1990) scheme, which includes eddy-induced velocity in addition to diffusion of
129 tracers along isopycnals. Macronutrients and oxygen are initialized from World Ocean Atlas 2013 version 2
130 dataset (Garcia et al., 2014a, b) and alkalinity is initialized using GLObal Ocean Data Analysis Project
131 (GLODAPv2; Olsen et al., 2016). Temperature and salinity are initialized from January-mean values from the
132 Polar Science Center Hydrographic Climatology, which is based on data from Levitus et al. (1998). Ecosystem
133 tracers, including iron, chlorophyll, dissolved organic and inorganic carbon are initialized from a previous CESM1
134 simulation.

135 The biogeochemistry component of POP2 is implemented using Marine Biogeochemistry Library (MARBL),
136 which is the most updated version of the previously implemented Biogeochemistry Elemental Cycle (BEC) model
137 (Long et al., 2021). The model includes key limiting nutrients (N, P, Si, Fe), three types of explicit phytoplankton
138 functional groups (diatoms, diazotrophs and nano/picophytoplankton), one implicit calcifier group, and one
139 zooplankton type. The C:N ratio for nutrient assimilation is fixed at 117:16 (Anderson and Sarmiento, 1994),
140 whereas P:C, Fe:C, Si:C and chlorophyll:C ratios are allowed to vary based on ambient nutrient concentrations.
141 The Fe:C ratio is allowed to change within a fixed range based on phytoplankton growth terms, loss terms, and
142 the iron uptake half-saturation constant for different phytoplankton groups (Moore et al., 2004). For each of the 3
143 phytoplankton groups the minimum allowed Fe:C ratio is 2.5 $\mu\text{mol mol}^{-1}$. The maximum allowed Fe:C ratio is 30
144 $\mu\text{mol mol}^{-1}$ for diatoms and small phytoplankton, and 60 $\mu\text{mol mol}^{-1}$ for diazotrophs due to their higher demand
145 for iron. The zooplankton Fe:C ratio is fixed at 3.0 $\mu\text{mol mol}^{-1}$. Individual nutrient limitation for phytoplankton is
146 assessed based on Michaelis-Menten nutrient uptake kinetics, which is a function of the specific nutrient
147 concentration and nutrient uptake half-saturation coefficient. The half-saturation coefficient is nutrient-specific
148 and phytoplankton-group specific. Nutrient limitation terms vary from 0 to 1, with 0 being the most limiting
149 nutrient. Multiple nutrient limitation follows Liebig's law of minimum, so that the nutrient limitation term with
150 minimum value limits phytoplankton growth rate (Long et al., 2021). Loss of phytoplankton in MARBL is
151 accounted for by grazing, mortality, and aggregation of sinking flocculants.

152 The main DFe sources considered in MARBL are atmospheric depositions, shelf sediments, riverine inputs, and
153 hydrothermal vents (Fig. S1). Globally, these sources of DFe account for 13.62 Gmol yr⁻¹, 19.68 Gmol yr⁻¹, 0.37
154 Gmol yr⁻¹, and 4.91 Gmol yr⁻¹, respectively (Long et al., 2021). Atmospheric sources of DFe are from dust and
155 black carbon depositions obtained from a fully coupled CESM2 simulation in hindcast mode at nominal 1° spatial
156 resolution as a part of the Coupled Model Intercomparison Phase 6 (CMIP6) contribution. Dust emissions and
157 transport/deposition are calculated, respectively, using the Community Land Model version 5 (CLM5) and
158 Community Atmosphere model version 6 (CAM6) in Whole Atmosphere Community Climate Model (WACCM)
159 configuration. The newly included Modal Aerosol Module version 4 (MAM4) in CAM6 includes dust in the
160 accumulation and coarse modes. Black carbon is emitted in the primary mode and transferred to accumulation
161 mode via aging (Liu et al., 2016). Monthly climatology of dust and black carbon for the year 2000 is used in
162 repeating mode. About 3.5% of dust is assumed to be iron with the solubility of iron depending on the ratio
163 between coarse and fine dust fluxes. This accounts for increasing iron solubility with increasing distance from
164 dust source regions. A constant solubility of 6% is assigned to iron derived from black carbon aerosols. In addition
165 to surface iron release, there is slow dissolution of sinking “hard” dust fraction (~98% of total dust) with depth
166 such that ~0.3% of dust will dissolve over 4000 m (Armstrong et al., 2002; Moore et al., 2004). For the rest of the
167 2% “soft” dust, remineralization takes place with a length-scale of 200 m. Sedimentary iron supply is based on
168 sub-grid scale bathymetry that depends on two factors: firstly, for reducing sediments, it is proportional to
169 particulate organic carbon fluxes in regions where these fluxes are larger than 3 g C m⁻² yr⁻¹; secondly, in oxic
170 sediments, it depends on constant low background fluxes and bottom current velocity, which accounts for
171 sediment resuspension. As a result, the main sources of sedimentary DFe are along continental shelves and
172 productive margins, with little contribution coming from the deep ocean. For the river source of DFe, discharge
173 data for the year 2000 from Global Nutrient Export from WaterSheds (GlobalNEWS, Mayorga et al., 2010) is
174 combined with constant DFe concentration of 10 nM. For hydrothermal vents, a constant flux of iron from the
175 grid boxes containing vents is applied so that the total hydrothermal vent iron flux is equal to approximately 5.0
176 Gmol yr⁻¹.

177 Iron input to the ocean is balanced by losses from biological uptake and scavenging. The biological uptake of iron
178 is based on the species-specific Fe:C ratio, which varies based on ambient DFe concentration, as discussed
179 previously. The biological uptake term also includes routing of phytoplankton iron to zooplankton based on its
180 feeding preference. Losses of iron from the biological pools are through mortality, aggregation, grazing upon
181 phytoplankton by zooplankton, as well as higher trophic grazing on zooplankton (Long et al., 2021). The
182 scavenging loss of DFe is expressed as a two-step process similar to the thorium scavenging model: involving the
183 calculation of the net adsorption rate to sinking particles and modification of this rate by the ambient iron
184 concentration (Moore and Braucher, 2008). The total sinking particles consist of particulate organic carbon,
185 biogenic silica, calcium carbonate, and dust, which strongly influence DFe scavenging in excess of ligand
186 concentrations. The particulate organic carbon is multiplied by 6 to account for the non-carbon portion of the
187 organic matter that can take part in scavenging. In CESM, scavenging increases non-linearly with DFe
188 concentration. About 90% of the scavenged iron enters the sinking particulate pool, while the rest is lost to
189 sediments. Along with the scavenging contribution, iron released from grazing and mortality of autotrophs and
190 zooplankton also enters the particulate iron pool. Remineralization of this sinking particulate iron replenishes DFe
191 and is parameterized as a function of sinking particulate organic carbon flux. This results in maximum

192 remineralization taking place within the upper 100 m where particulate organic carbon flux is the highest.
 193 Additionally, slow desorption of sinking particulate iron also releases DFe at depths and is calculated using a
 194 constant desorption rate of $1.0 \times 10^{-6} \text{ cm}^{-1}$ for particulate iron. The model also includes an explicit ligand tracer
 195 for complexing Fe, with ligand sources being from particulate organic carbon remineralization and dissolved
 196 organic matter production. Ligand sinks involve scavenging, uptake by phytoplankton, ultraviolet radiation, and
 197 bacterial uptake or degradation (Long et al., 2021). An overview of the different sources and sinks of DFe used
 198 in CESM-MARL is given in Figure 1.



199
 200 **Figure 1: Schematic representation of iron cycle in the ocean component of the CESM model. The texts/boxes/arrows**
 201 **in black show the main processes affecting the dissolved iron pool, while those in red further show what controls the**
 202 **processes impacting the dissolved iron pool. POC (DOC): particulate (dissolved) organic carbon, bSi: biogenic silica.**

203
 204 This study is based on 5 sets of simulations for identifying contributions from different sources of DFe: control
 205 simulation (CTRL); and simulations that individually remove DFe supply from atmospheric depositions (NATM),
 206 sediments (NSED), rivers (NRIV) and hydrothermal vents (NVNT). Differences between CTRL and NATM
 207 simulations indicate the biogeochemical impacts solely due to atmospheric deposition of DFe and is referred to
 208 as ATM. Similarly, biogeochemical impacts solely from sedimentary, river and hydrothermal DFe sources are,
 209 respectively, referred to as SED, RIV and VNT cases. Simulations have been conducted in hindcast mode for 60
 210 years using forcing from the Coordinated Ocean-ice Reference Experiments version 2 (CORE-II) dataset for the

211 years 1948-2007 (Large & Year, 2009). The CORE-II data includes interannual variability and consists of 6-
212 hourly temperature, air density, specific humidity, 10 m wind-speeds, and sea-level pressure from National
213 Centers for Environmental Prediction/ National Center for Atmospheric Research (NCEP/NCAR) Reanalysis
214 (Kalnay et al., 1996). Daily shortwave and longwave radiation are taken from Goddard Institute for Space Studies-
215 International Satellite Cloud Climatology Project radiative flux profile data (GISS-ISCCP-FD) (Zhang et al.,
216 2004). Monthly precipitation is combined Global Precipitation Climatology Project (GPCP, Huffman et al., 1997)
217 and Climate Prediction Center Merged Analysis of Precipitation (CMAP, Xie & Arkin, 1997) data. Monthly
218 streamflow since 1948 used in this study has been previously derived from gauge data, where linear regression
219 was also employed using CLM3 model streamflow to fill-in missing data (Dai et al., 2009). The present study
220 uses the last 10 years of simulations, given its focus on impacts of DFe sources on biogeochemistry of the upper
221 100 m of the oceans at seasonal scale.

222

223 **2.2 Observation data**

224 Monthly climatology for ocean temperature, salinity and nutrients have been obtained from World Ocean Atlas
225 2018 (WOA18) at $1^{\circ}\times 1^{\circ}$ spatial resolution (Garcia et al., 2019). Monthly surface chlorophyll concentrations have
226 been obtained from the European Space Agency Ocean Color Climate Change Initiative (OC-CCI) version 5 at 4
227 km spatial resolution for the period 2003-2020 (Satyendranath et al., 2019). OC-CCI merges ocean color
228 information from multiple sensors: Moderate Resolution Imaging Spectroradiometer (MODIS, 2002-present),
229 Sea-Viewing Wide Field-of-View Sensor (SeaWiFS, 1997-2010), MEidium Resolution Imaging Spectrometer
230 (MERIS, 2002-2012) and Visible Infrared Imaging Radiometer (VIIRS, 2012-present). The product is bias-
231 corrected and quality-controlled, yielding much lower data gaps compared to individual sensors. Monthly
232 climatology of mixed layer depth (MLD) gridded at $1^{\circ}\times 1^{\circ}$ spatial resolution has been obtained from Argo profiles
233 based on a hybrid algorithm that calculates a suite of MLDs using several criteria, such as gradient/threshold
234 method, maxima or minima of a particular property, intersection with seasonal thermocline (Holte et al., 2017).
235 The resulting patterns are analysed to yield final MLD estimates. To explore ocean surface circulation, Ocean
236 Surface Current Analysis Real-time (OSCAR) data at $0.33^{\circ}\times 0.33^{\circ}$ spatial resolution and 5-day temporal resolution
237 has been used. Horizontal velocities are measured using sea surface heights, ocean surface winds, and sea surface
238 temperatures, thereby accounting for flows due to geostrophic balance, Ekman dynamics, and thermal wind
239 (Dohan & Maximenko, 2010).

240

241 To examine the ability of CESM to realistically simulate the variation in DFe concentrations in the upper 100 m
242 over the northern IO, this study uses DFe profile compilations by Tagliabue et al. (2012) and the GEOTRACES
243 Intermediate Data Product 2021 (Schlitzer et al., 2021). To these, published data from Moffett et al. (2015) has
244 also been added, comprising DFe data collected in the AS during September 2007. The DFe estimated in these
245 data are based on filtration of seawater through filter sizes between 0.2-0.45 μm .

246

247 **3 Results and discussions**

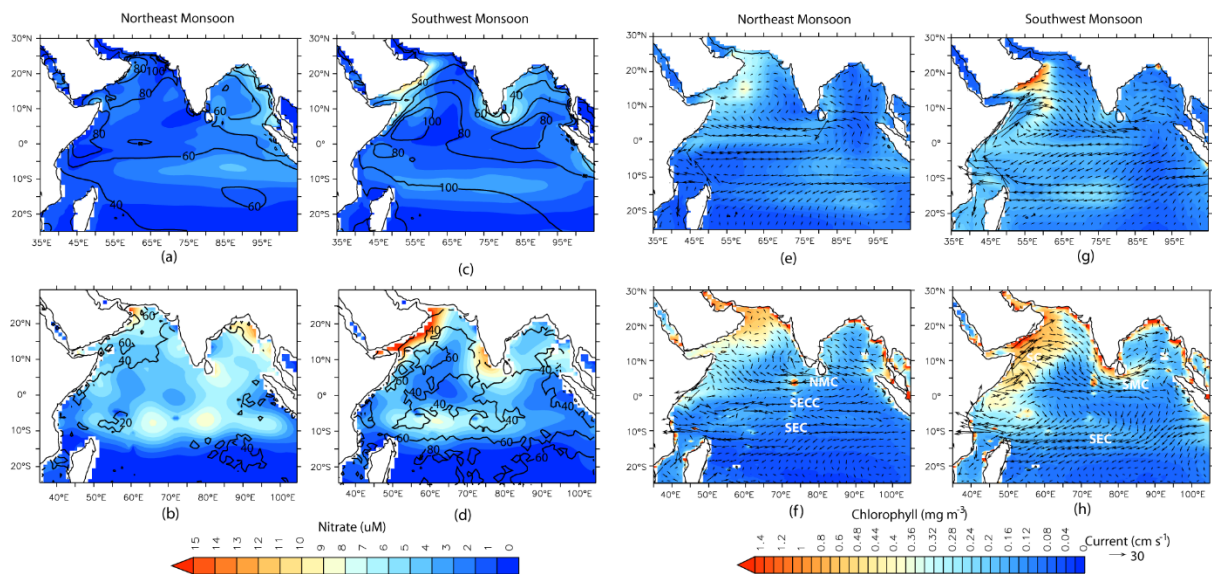
248 First, the performance of CESM-POP2 simulations with respect to observations over the northern IO is examined.
249 Next, the contributions of different DFe sources to upper ocean DFe concentrations, phytoplankton blooms and

250 patterns of nutrient limitations is discussed. Finally, the paper explores how different sources of DFe can influence
251 the total DFe budget across selected biophysical regimes over the northern IO.

252 **3.1 Model evaluation**

253 In this section CESM simulation (for CTRL case) of physical parameters as well as nitrate and chlorophyll
254 concentrations over the upper 100 m of the northern IO is evaluated. Except for MLD, ocean currents, and
255 chlorophyll, all modeled parameters have been compared with WOA18 observations. Simulated MLDs are
256 compared with Argo-based values of Holte et al. (2017), ocean currents are compared with OSCAR data, and
257 chlorophyll concentrations are compared with OC-CCI observations. In general, CESM shows good
258 correspondence with observations of seasonal cycle of temperature, salinity and MLD. However, there is a
259 positive temperature and salinity bias over IO (Figs. S2 and S3 in the Supplement). This warm bias over IO differs
260 from the previous version of CESM, which has a cold bias in this region (Danabasoglu et al., 2020). Figure 2
261 shows seasonal climatology in CESM simulations and observations, for MLD, nitrate concentrations, surface
262 ocean currents, and chlorophyll concentrations. Overall, CESM simulates the main features of surface ocean
263 circulation and spatio-temporal variations in MLD well. There are some deviations, such as a much stronger
264 simulated Somali Current along the northeast coast of Africa, especially during the southwest monsoon season,
265 which can lead to strong advection of upwelled nutrients away from this region. CESM also simulates a stronger
266 South Equatorial Current during southwest monsoon, which occupies a broader region compared to observations
267 and leads to a stronger westward flow in the model between 0-5°S latitude. The net result of the warm and positive
268 salinity bias is that CESM simulates much deeper MLD than observations throughout the year across the study
269 domain. Averaged annually, the largest overestimation (of ~40 m) is over the equatorial IO particularly during the
270 spring and fall intermonsoon months, when the Wyrki Jet is prevalent over the region (Figs. S3 e-f). Additionally,
271 MLD overestimation of ~45 m is also seen over the AS during February-March and the southern tropical IO
272 during September-October, both associated with winter-convection.

273 With respect to the seasonal cycle of nitrate, CESM has the least bias over AS followed by BoB (Figs. 2a-d and
274 S4), but its performance is comparatively lower over the equatorial IO and southern tropical IO. For example,
275 WOA18 data shows the highest value of nitrate over southern tropical IO in January, whereas in CESM simulation
276 the highest nitrate concentration is shifted to April-June associated with mixed layer deepening. On the other
277 hand, CESM simulates a much weaker seasonal cycle of nitrate over the equatorial IO compared to WOA18
278 observations. These regions, over southern tropical IO, and the equatorial IO, where CESM fares poorly also have
279 fewer nutrient profile observations compared to AS and BoB. For example, no more than 10 nitrate observations
280 are available in a grid-point over the southern tropical IO and equatorial IO, whereas there are several grid-points
281 over the AS where more than 30 observations are available. Overall, CESM simulations underestimate nitrate
282 with respect to WOA18 data for the upper 100 m of the water column.



283

284 **Figure 2: Comparison of CESM-CTRL simulated variables (upper panels) with observations (lower panels) for**
 285 **northeast monsoon (a,b,e,f) and southwest monsoon (c,d,g,h). Shading in (a-d) are nitrate concentrations averaged for**
 286 **upper 100 m and the black contours are the mixed layer depth (m). Shading in (e-h) are surface chlorophyll**
 287 **concentrations and the vectors are the surface currents. SEC: South Equatorial current, SECC: South Equatorial**
 288 **Counter Current, NMC: Northeast Monsoon Current, SMC: Southwest Monsoon Current, SC: Somali Current.**

289

290 Turning to chlorophyll concentrations, CESM simulations capture the main characteristics of the seasonal cycle
 291 and its spatial distribution over the northern IO (Figs. 2e-h and S4), with certain biases and shifts in the timing of
 292 the peak blooms. For example, over the BoB, the model has difficulty in capturing the temporal evolution of
 293 chlorophyll concentrations. Over the AS and the equatorial IO, peak bloom in the simulations occurs in September,
 294 in contrast to July in the observations. Similarly, over the southern tropical IO, the peak bloom is delayed in the
 295 model to October as compared to its appearance in July in observations. Most of the AS and the BoB show
 296 underestimation ($\sim -60\%$) in simulated chlorophyll concentration with respect to OC-CCI values. Such
 297 underestimation of major nutrients and chlorophyll over most of the northern IO are common to many modelling
 298 studies where coastal regimes and mesoscale processes are not adequately captured without finer spatial resolution
 299 (e.g., Dutkiewicz et al., 2012; Ilyina et al., 2013; Long et al., 2021; Moore et al., 2013b; Pham & Ito, 2021). For
 300 example, a modelling study by Resplandy et al. (2011) has shown that eddy-induced vertical transport is
 301 responsible for $\sim 40\%$ of nitrate fluxes in the winter convection regions of the AS during the late northeast
 302 monsoon. The study also showed that mesoscale eddies can account for 65-91% of vertical and lateral advection
 303 of nitrate in the upwelling regions of the AS during the southwest monsoon. Additionally, the positive MLD bias
 304 simulated by CESM can trigger light limitation of phytoplankton growth, leading to underestimation of
 305 chlorophyll. If the threshold depth for photosynthesis is considered as the depth of the isolume given by 0.415
 306 $\text{mol quanta m}^{-2} \text{d}^{-1}$ ($Z_{0.145}$, Boss & Behrenfeld, 2010; Letelier et al., 2004), then the CESM simulated MLD is
 307 deeper than the $Z_{0.145}$, leading to light limitation of phytoplankton growth over the entire AS and large parts of
 308 BoB throughout the year (Fig. S5). During the southwest monsoon, almost the entire domain experiences light
 309 limitation, especially off the coast of Somalia and the southern tropical IO.

310 CESM simulations of DFe are evaluated next, using all available *in situ* DFe concentration data for upper 20 m
 311 of the ocean, for different seasons. In addition, distribution of DFe along selected transects for the upper 100 m

312 are studied: (1) CLIVAR cruise 109N along the eastern IO during April 2007; and (2) GEOTRACES cruises GI-
313 01, GI-02, GI-03, GI-04 and GI-05. While CESM simulates the general pattern of DFe distribution over the
314 northern IO reasonably well, DFe variation with depth and with increasing distance from the coast is stronger in
315 simulations than in observations. For upper 20 m, Pearson product-moment correlation coefficient calculated
316 between observed and simulated DFe concentrations is 0.62 (Figs. 3a-d). The coefficients for correlation between
317 observed and simulated DFe for GEOTRACES and CLIVAR transects vary between 0.64 and 0.38 (Fig. 3e). All
318 these correlation coefficients are significant at 95% confidence level based on Student's t-test with n-2 degrees of
319 freedom, where n is the sample size. This indicates that CESM is able to reproduce the north-to-south gradient in
320 DFe concentrations, the comparatively low DFe concentration west of 65°E over the AS, as well as increases in
321 DFe with depth over both the eastern and western IO reasonably well. Overall, CESM simulates positive bias in
322 DFe concentration over the study domain (see Table S1). A closer look at the pattern of bias in simulated DFe
323 reveals several features: (1) the magnitude of the positive bias is much lower to the south of 5°S latitude compared
324 to the north, (2) CESM simulated DFe has low magnitude of negative bias to the west of 60°E longitude over the
325 AS near the dust sources and (3) Coastal and open oceans experience similar magnitudes of positive DFe bias
326 throughout the domain, implying that DFe bias might be stemming from multiple sources.

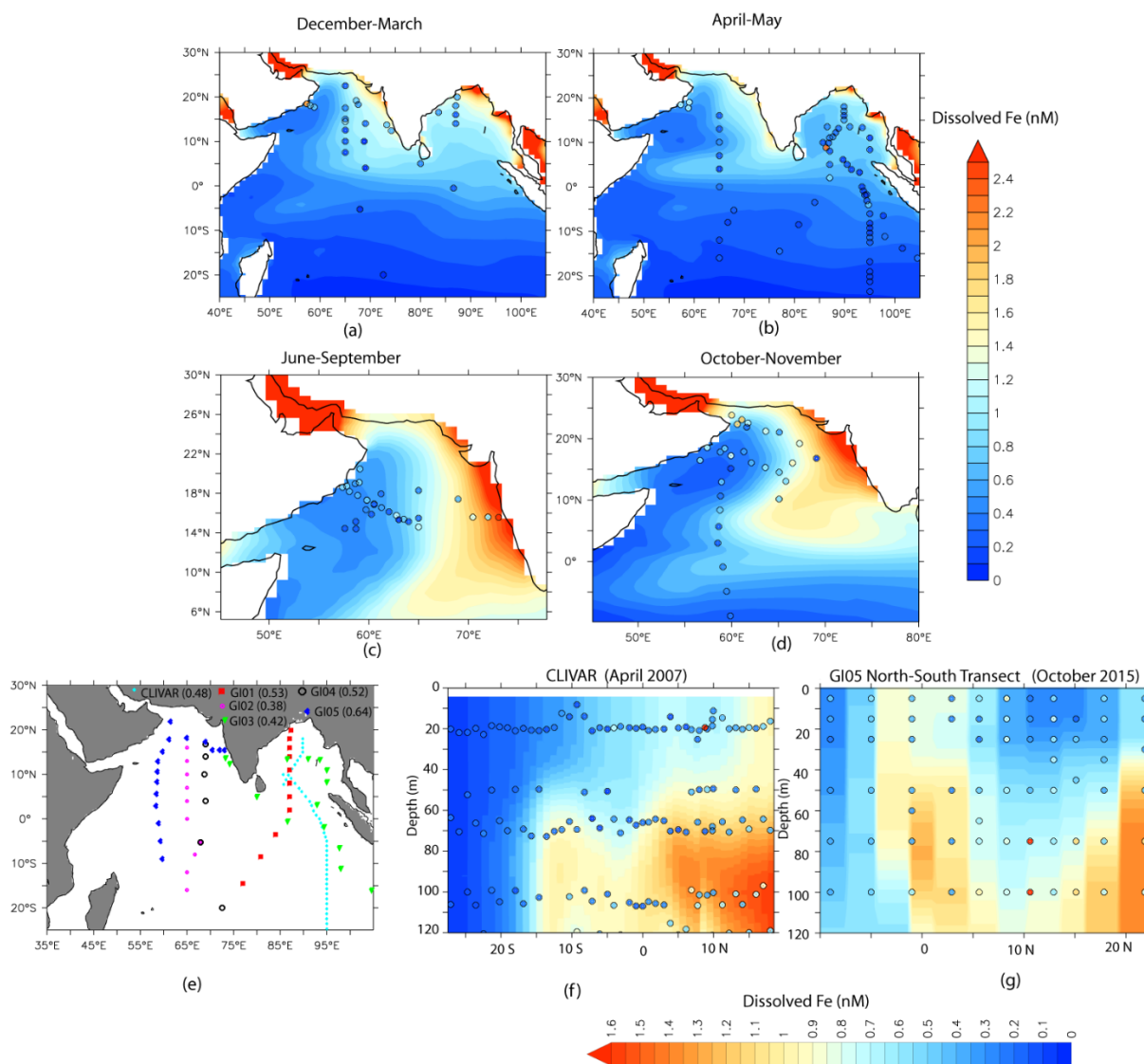
327 Figures 3 f and g show two examples of variation of DFe distribution with latitude and depth along the eastern
328 and western IO, respectively. The model overestimates DFe values, especially to the north of the equator and at
329 depths greater than 60 m. Such overestimation of DFe over the northern IO in CESM could result from a variety
330 of factors, like source strength, assumed solubility of iron, and uncertainties in the removal of DFe by biological
331 uptake as well as scavenging. With respect to source strength, dust deposition is one possible factor that can lead
332 to overestimation of simulated DFe. Using Dust Indicators and Records of Terrestrial and MARine
333 Palaeoenvironments (DIRTMAP) version 2 database of modern day dust deposition (Kohfeld & Harrison, 2001)
334 an attempt has been made here to understand CESM bias in dust deposition over AS. Median dust deposition
335 values from DIRTMAP ranges between $\sim 14 \text{ g m}^{-2}\text{yr}^{-1}$ over the western AS (40°-60°E), $\sim 7 \text{ g m}^{-2}\text{yr}^{-1}$ over the central
336 AS (60°-70°E) and $\sim 20 \text{ g m}^{-2}\text{yr}^{-1}$ over the eastern AS (70°-80°E) (Kohfeld & Harrison, 2001). Corresponding
337 median values of dust deposition over these locations from CESM model are $5 \text{ g m}^{-2}\text{yr}^{-1}$, $9 \text{ g m}^{-2}\text{yr}^{-1}$ and $14 \text{ g m}^{-2}\text{yr}^{-1}$
338 respectively, indicating a general underestimation of dust deposition by CESM, especially to the west of 60°E
339 longitude. Over the eastern IO, using mixed layer dissolved Al concentrations dust depositions have been
340 estimated to be $0.2\text{-}3.0 \text{ g m}^{-2}\text{yr}^{-1}$ between 20°S to 10°N latitude (Grand et al., 2015). In a separate study, based on
341 Al concentrations in the aerosol, Srinivas and Sarin (2013) have estimated dust dry-deposition flux of $0.3\text{-}3.0 \text{ g m}^{-2}\text{yr}^{-1}$
342 over BoB. Dust deposition from CESM is on the lower end of this range varying from $1.1 \text{ g m}^{-2}\text{yr}^{-1}$ over
343 the northern BoB to $0.2 \text{ g m}^{-2}\text{yr}^{-1}$ near the equator. Sediment traps deployed at shallow depths over the BoB have
344 recorded annual lithogenic fluxes varying from the northern to the southern bay as $\sim 15 \text{ g m}^{-2}\text{yr}^{-1}$ ($\sim 89.5^\circ\text{E}$, 17.5°N)
345 to $\sim 4 \text{ g m}^{-2}\text{yr}^{-1}$ (87°E , 5°N) (Unger et al., 2003). The corresponding variations in CESM dust deposition are $\sim 9 \text{ g m}^{-2}\text{yr}^{-1}$,
346 to $\sim 2 \text{ g m}^{-2}\text{yr}^{-1}$. Thus, overall, there is some underestimation of dust deposition over the northern IO, which
347 might not explain positive DFe bias in CESM simulations. However, there is a possibility of fractional solubility
348 of Fe from dust having an impact on DFe derived from atmospheric sources. Over the AS, percentage solubility
349 of aerosol has been reported to vary between 0.02 and 0.43% (Srinivas et al., 2012). Considering that Fe constitutes
350 3.5% of dust by weight and using 0.02% and 0.5% as the lower and upper bounds to Fe solubility, the total fluxes
351 of soluble Fe based on CESM dust deposition are calculated. The calculated iron flux ranges from 0.002 (0.04)

352 $\mu\text{mol m}^{-2} \text{d}^{-1}$ over the western AS to 0.01 (0.35) $\mu\text{mol m}^{-2} \text{d}^{-1}$ over the eastern AS for 0.02% (0.5%) solubility. The
353 corresponding ranges of soluble Fe flux from CESM is 0.05 $\mu\text{mol m}^{-2} \text{d}^{-1}$ in the west to 0.8 $\mu\text{mol m}^{-2} \text{d}^{-1}$ in the
354 eastern AS. Again, using median dust deposition values from DIRTMAP data and assuming 0.5% iron solubility,
355 soluble Fe fluxes vary from 0.12 to 0.17 $\mu\text{mol m}^{-2} \text{d}^{-1}$ from west to east AS. It is therefore clear that CESM model
356 input of soluble Fe from atmosphere is overestimated compared to observations. This inference does not change
357 even after adding the contribution of black carbon (after assuming 6% solubility of Fe) to the atmospheric iron
358 flux. This is because fractional solubility of Fe in CESM varies from 1.2% over northwestern AS to ~5% over the
359 southern AS. Ship-based measurements, on the other hand, have observed that high levels of CaCO_3 in the dust
360 over the AS acts as a neutralizing agent, leading to much lower aerosol solubility (Srinivas et al., 2012).
361 Additionally, for the GI05 transect (Fig. 3g), DFe concentration reduces drastically in the NATM case (Fig. S6 a-
362 c), indicating that dust deposition and its solubility is the major factor contributing to the simulated levels of DFe
363 and its biases.

364 The impact of dust solubility on DFe concentration, however, does not explain the positive biases in simulated
365 DFe over the BoB. The percentage solubility of aerosol iron measured over the BoB is high, varying between
366 2.3% and 24%, due to presence of acid species from anthropogenic activities (Srinivas et al., 2012). This leads to
367 much higher soluble iron deposition than that is obtained from CESM. For example, in CESM the soluble Fe flux
368 over BoB varies from ~0.05 to 0.35 $\mu\text{mol m}^{-2} \text{d}^{-1}$, whereas, calculated soluble Fe flux varies from 0.06 to above 1
369 $\mu\text{mol m}^{-2} \text{d}^{-1}$. Thus, atmospheric supply of iron is possibly underestimated over the BoB. It is, therefore, quite
370 possible that this positive bias in DFe stems from either sedimentary or river sources. In fact, comparing CTRL
371 simulation with NATM and NSED along the CLIVAR transect in Figure 3f, reveals considerable contribution of
372 sedimentary sources of DFe, especially at depth greater than 60 m (Fig. S6 d-f). Furthermore, the latitudinal
373 change in salinity along this transect closely follows the latitudinal pattern of change in DFe from NATM case,
374 but not DFe from NSED case. To examine this, DFe from NATM and NSED cases and salinity from CTRL case
375 have been taken along the CLIVAR transect from depths greater than 60 m and have been detrended. The
376 correlation between DFe from NATM and salinity is -0.75 indicating that non-atmospheric sources of DFe is
377 associated with fresher water transported from the coastal regions. The corresponding correlation between DFe
378 from NSED and salinity is -0.16 indicating that non-sedimentary sources of DFe has no salinity dependence. The
379 underestimation of atmospheric iron deposition along with salinity-dependence of DFe from the NATM case
380 together indicates that enhanced transport of sediments from continental margins is likely to be the source of DFe
381 bias along the CLIVAR transect. One possible explanation is that the low resolution of the model is unable to
382 capture the high velocity of the coastal currents that may limit the spreading of sediments from the coastal regions
383 to the open oceans. The simulated coastal current is weaker than OSCAR observations during April, when the
384 CLIVAR measurements were undertaken (Fig. S6 g-h). This can lead to greater diffusive spreading of iron from
385 the coast into the open ocean. Such an effect of model resolution has been previously shown to result in a higher
386 sedimentary contribution to DFe off the northwest Pacific and southwest Atlantic ocean (Harrison et al., 2018).

387

388



389

390 **Figure 3: Comparison of CESM-CTRL simulated DFe (shading) with the observations (filled circles) compiled from**
 391 **various cruises. The spatial distribution maps in (a-d) consider season-wise DFe distribution averaged over the upper**
 392 **20 m. (e) The different cruise tracks from which DFe measurements have been used are marked. The numbers within**
 393 **the parentheses are the correlation coefficients between observed and simulated DFe for each cruise. The vertical**
 394 **transects in (f-g) show DFe gradients in the water column over (f) the eastern Indian Ocean and (g) the western Indian**
 395 **Ocean.**

396 With respect to loss terms, biases in Fe uptake and scavenging can impact simulated DFe concentrations,
 397 especially in the surface waters. To account for Fe uptake by phytoplankton, particulate organic carbon export
 398 fluxes at 100 m calculated from ^{234}Th fluxes have been used in conjunction with Fe:C ratios. Since the cellular
 399 Fe:C ratio varies widely depending on external DFe availability and phytoplankton species composition, a lower
 400 bound of $6 \mu\text{mol mol}^{-1}$ and an upper bound of $50 \mu\text{mol mol}^{-1}$ have been considered. The lower bound is based on
 401 measurements over the eastern IO (Twining et al., 2019) where oligotrophic conditions are encountered. The
 402 upper bound is based on measurements over the tropical North Atlantic where high dust deposition leading to
 403 high surface DFe concentration prevails (Twining et al., 2015). Combining Fe:C values with particulate organic
 404 carbon export fluxes from JGOFS cruises (Buesseler et al., 1998) yields Fe uptake by phytoplankton varying
 405 between ~ 0.0004 and $\sim 0.0035 \mu\text{mol m}^{-3} \text{d}^{-1}$ for all seasons over the AS. Phytoplankton Fe uptake from CESM
 406 over the AS varies between ~ 0.0001 and $\sim 0.002 \mu\text{mol m}^{-3} \text{d}^{-1}$, which are on the lower end of observation-based

407 values. Over the BoB, phytoplankton Fe uptake varies between ~ 0.00002 and $\sim 0.004 \mu\text{mol m}^{-3} \text{d}^{-1}$ based on
408 available POC measurements (Anand et al., 2017; 2018). The corresponding ranges of CESM simulated DFe
409 uptake are ~ 0.0002 to $\sim 0.001 \mu\text{mol m}^{-3} \text{d}^{-1}$, which is within the range of values calculated from observations. With
410 respect to scavenging losses, based on particulate Fe value from the eastern tropical South Pacific and ^{234}Th fluxes
411 over the AS, Chinni and Singh (2022) estimated abiotic removal of 0.001 - $0.005 \mu\text{mol m}^{-3} \text{d}^{-1}$ for the upper 100 m.
412 In the present simulations, average scavenging removal is $\sim 0.003 \mu\text{mol m}^{-3} \text{d}^{-1}$ over both the AS and BoB (range:
413 0.002 to $0.026 \mu\text{mol m}^{-3} \text{d}^{-1}$) and reduces to less than $0.001 \mu\text{mol m}^{-3} \text{d}^{-1}$ to the south of the equator. Overall, Fe
414 uptake by phytoplankton is possibly underestimated over the AS, which can contribute to some overestimation of
415 DFe in the surface waters over this region. Over BoB, Fe uptake is within the range of observation-based values.
416 Scavenging removal simulated by CESM is also within the range of observation-based values and is possibly not
417 contributing to DFe bias in CESM.

418 To summarize, the ocean component of CESM has deeper MLD than observations, underestimates nitrate and
419 chlorophyll, and overestimates DFe concentrations. Together, this can result in weaker iron-limitation in the
420 simulations compared to observations. Over the AS, the positive bias in simulated DFe is present mostly to the
421 east of 60°E longitude and can be related to the higher solubility of atmospheric iron in CESM compared to the
422 observations. Over the BoB, DFe bias likely originates from enhanced transport of sedimentary iron from
423 continental shelf margins. To the west of 60°E , simulated DFe has negative bias of low magnitude, possibly
424 because underestimation of dust deposition is counterbalanced by overestimation of iron-solubility. Over the
425 southern tropical IO, the magnitude of bias is also low compared to the rest of the study domain. Still, the model
426 simulates spatial and temporal patterns of ocean physical features, as well as variations in chlorophyll
427 concentrations, nitrate, and DFe concentrations over the northern IO reasonably well. This gives confidence in
428 using the model to study the iron cycle over the region. Taking the above understanding of strengths and
429 shortcomings of the model into account, the importance of different DFe sources with respect to biogeochemistry
430 of the upper 100 m of the northern IO is explored next.

431

432 **3.2 Contribution of multiple iron sources**

433

434 Figure 4 summarizes the contributions of different sources to annually averaged DFe concentration. Source-wise
435 DFe contributions for northeast and southwest monsoons are shown in Figs. S7 and S8, respectively. Overall, the
436 relative contribution from different sources to DFe is nearly the same across different seasons, except for the
437 somewhat higher contribution of atmospheric DFe during southwest monsoon compared to northeast monsoon.
438 This is because the arid and semi-arid regions surrounding the northern IO experiences maximum dust activity
439 from late spring to early southwest monsoon months (e.g., Banerjee et al., 2019; Léon and Legrand, 2003). In the
440 annual average, atmospheric deposition is the most important source of DFe over the northern IO and contributes
441 well above 50% of the total DFe concentrations (ATM case in Fig. 4b). Furthermore, atmospheric deposition
442 contributes more than 70% of DFe supply over most of the AS, southern BoB, and the equatorial IO. The location
443 of the intertropical convergence zone during northeast monsoon ($\sim 10^\circ\text{S}$ latitude) determines the southern limit of
444 the influence of atmospheric deposition because southwards of the intertropical convergence zone there is a rapid
445 reduction in DFe concentrations. Dust is the predominant contributor to the atmospheric deposition flux of iron.

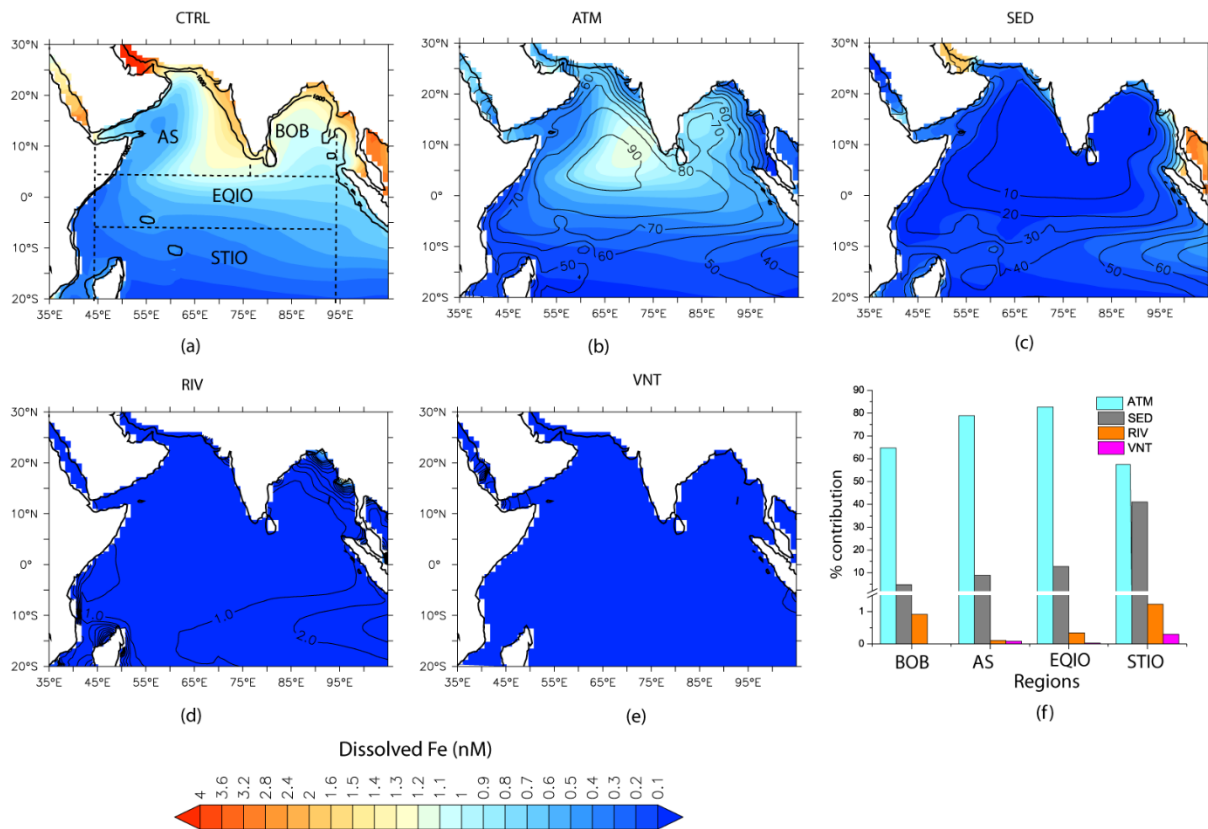
446 Over the northern AS, dust is mostly transported from Iran, Pakistan, Afghanistan, and the Arabian Peninsula,
447 whereas over southern AS dust from north-eastern Africa also becomes important (Jin et al., 2018; Kumar et al.,
448 2020). Over northern and southern BoB, the major sources of dust are the Indo-Gangetic Plain and northeast
449 Africa, respectively (Banerjee et al., 2019). Eastwards of 90°E, black carbon contributes ~50% to atmospheric
450 DFe flux during the northeast monsoon (not shown). The source of black carbon in this region is biomass burning
451 and fossil fuel combustion transported from the Indo-Gangetic Plain and Southeast Asia (Gustafsson et al., 2009;
452 Moorthy & Babu, 2006).

453 The second largest source of DFe is from continental shelf sediments (Fig. 4c), which become dominant in the
454 vicinity of the shelves. High sedimentary sources of DFe are characteristic of the Andaman Sea where incoming
455 rivers can contribute $\sim 600 \times 10^6 \text{ T yr}^{-1}$ of sediments (Robinson et al., 2007). It has been estimated that terrestrial
456 sources contribute more than 80% to total organic carbon in the inner shelf region of the Gulf of Martaban,
457 adjacent to the Andaman Sea (Ramaswamy et al., 2008). Elsewhere, sedimentary contributions of ~20% to overall
458 DFe are found in CESM runs along the northern part of west coast of India and the eastern BoB. Within Ganga-
459 Brahmaputra system, which is responsible for discharge of $\sim 11 \times 10^8 \text{ T yr}^{-1}$ of sediments, only 10% of sediments
460 is estimated to be transported longshore, with most of the sediments accumulating within the shelf and
461 subterranean canyon (Liu et al., 2009). Over the open ocean, sedimentary sources are most important within 10°-
462 15°S latitude where the South Equatorial Current is responsible for ~50% of DFe supply via advection from the
463 Indonesian shelf. During southwest monsoon, sedimentary contribution by the South Equatorial Current extends
464 farther westward (~70°E longitude, Fig. S8c) compared to the northeast monsoon (~80°E longitude, Fig. S7c).
465 Signatures of elevated Al due to sedimentary contribution is seen in ship-borne measurements (Grand et al., 2015;
466 Singh et al., 2020). In fact, such measurements have shown that the South Equatorial Current separates DFe-rich
467 oxygen-poor water of the northern IO from the DFe-poor oxygen-rich water of the southern tropical IO (Grand et
468 al., 2015).

469 River sources contribute negligibly to total DFe concentrations (Fig. 4d), except in the immediate vicinity of the
470 mouths of large river systems in the northeast BoB: the Ganges-Brahmaputra and the Irrawady-Sittang-Salween.
471 This can arise from the fact that DFe from river is mostly concentrated within the fresher upper 30 m of the water
472 column to the north of 21°N over the BoB and also due to high scavenging losses of iron at the river mouth.
473 Hydrothermal vents also contribute negligibly to DFe concentrations in the upper 100 m (Fig. 4e). The
474 hydrothermal vents supplying DFe (often excess of 1.5 nM) in the northern IO are located in the Central Indian
475 Ridge and the Carlsberg Ridge (Chinni & Singh, 2022; Nishioka et al., 2013; Vu & Sohrin, 2013), and largely
476 influence DFe concentrations below 1000 m depths. The shallowest hydrothermal plumes enriched with Fe are
477 located between ~650-900 m in the Gulf of Aden (Gamo et al., 2015), overlapping with the depth range at which
478 the Red Sea watermass spreads along the western IO (Beal et al., 2000). Since this watermass occupies
479 progressively deeper depths with distance, sliding underneath Persian Gulf waters, surface DFe values are not
480 impacted by these shallower vents. This is in concordance with simulations of Tagliabue et al. (2010) where,
481 following 500 years of model integration, hydrothermal vents increase globally averaged DFe concentrations by
482 only ~3% in the depth range of 0-100 m.

483 The average contribution of different sources of iron to the upper 100 m is summarized for different open ocean
484 regions over the northern IO in Fig. 4f. Annually averaged atmospheric deposition is clearly the most important
485 source of DFe throughout the northern IO. The exception to the dominant role of atmospheric deposition is the

486 southern tropical IO, where sedimentary sources of iron contribute ~40% to the upper ocean iron budget. Based
 487 on the analysis of origin of bias in simulated DFe concentrations in Section 3.1, it is likely that contribution of
 488 atmospheric sources to upper 100 m DFe concentration is overestimated over the eastern AS and the contribution
 489 of sedimentary sources to upper 100 m DFe concentration is overestimated over the BoB. Averaging over the
 490 entire domain, atmospheric source contributes ~67% to the upper 100 m DFe concentration. On masking out the
 491 region to the east of 65°E longitude over the AS, where the highest positive bias of DFe from dust has been noted,
 492 it is seen that atmospheric source contributes ~65% to the upper 100 m DFe concentration. Again, averaging over
 493 the study domain, sedimentary source contributes ~30% to the upper 100 m DFe concentration. On masking out
 494 BoB, where positive bias of DFe from sedimentary sources has been identified in Section 3.1, it is seen that
 495 sedimentary source contributes ~33% to the upper 100 m DFe concentration. Thus, while biases in the source
 496 strength might regionally impact the percentage contribution of DFe from various sources to the northern IO, the
 497 overall conclusion of atmospheric source being the most important for upper ocean DFe over the northern IO,
 498 followed by sedimentary sources, does not change. River contribution is generally ~1%, with slightly higher
 499 contributions in BoB and the southern tropical IO. Hydrothermal vents make negligible contributions throughout
 500 the northern IO. Adding these four sources of DFe estimated from CESM experiments does not yield the full
 501 100% of the DFe source, owing to non-linear effects associated with iron removal processes as well as
 502 complexation by organic ligands.



503
 504
 505
 506
 507
 508
 509
 510
 511

Figure 4: Contribution of different sources of DFe averaged over the year to the total DFe concentrations over the upper 100 m. Shading in (a) shows total DFe concentration with all sources included and shadings in (b-e) shows DFe concentrations arising from individual source. Contours in (b-e) show the percentage contribution of each source to total DFe concentrations. (f) Bar chart depicting source-specific DFe contribution (in %) over Bay of Bengal (BOB), Arabian Sea (AS), equatorial IO (EQIO), and the southern tropical IO (STIO). These regions are marked by the dashed boxes in (a). The thick black contour in (a) traces the 1000 m bathymetry.

512 3.3 Phytoplankton responses to multiple iron sources

513 In this section, the impact of different sources of DFe on phytoplankton growth is examined. Since river and
514 hydrothermal sources make negligible contributions to the upper ocean iron concentrations, as shown above, these
515 are not considered further.

516 3.3.1 Responses to atmospheric depositions

517 During the northeast and southwest monsoons, atmospheric DFe brings about increases in column-integrated
518 chlorophyll concentrations over most of the northern IO (Figs. 5 a and c). The largest column-integrated positive
519 response is seen in the western AS (west of ~65°E longitude) throughout the year, where atmospheric DFe
520 accounts for more than ~20% of the column-integrated chlorophyll concentration and more than 50% of surface
521 chlorophyll concentration (Fig. S9). This region comes under the influence of upwelling during the southwest
522 monsoon and mixed layer deepening due to winter convection during the northeast monsoon, which can supply
523 macronutrients required for phytoplankton growths (Madhupratap et al., 1996; Morrison et al., 1998). The other
524 region displaying a strong positive response is the southern tropical IO during June-September, where atmospheric
525 DFe contributes ~20% (~35%) of the column (surface) chlorophyll concentration. This is the time of the year
526 when deep mixed layer leads to entrainment of nutrients into the surface layers (Košić et al., 2009; Lévy et al.,
527 2007). In contrast, there are some regions, like the northern and western AS, the west coast of India and large
528 parts of the BoB and the eastern IO, which in spite of receiving high atmospheric DFe hardly experience any
529 chlorophyll response. These regions show <1% increase in column chlorophyll concentrations and generally
530 coincide with high sedimentary iron input. This is discussed further in Section 3.3.3

531 Species-wise decomposition shows that the increases in chlorophyll during both northeast and southwest
532 monsoons are driven by increases in diatoms and declines in small phytoplankton (Fig. 6). For example, over the
533 western AS and southern tropical IO, diatoms increase by at least 40% and small phytoplankton populations
534 decline by at least 50%. An exception is the equatorial IO, where the positive response of chlorophyll arises from
535 growth of small phytoplankton. In general, this region has very low levels of macronutrients and is dominated by
536 picoplankton (Vidya et al., 2013). Those regions exhibiting <1% increase in phytoplankton in response to
537 atmospheric DFe, in contrast, are characterized by proliferation of small phytoplankton and reductions of diatoms.
538 Although diazotrophs show positive response to atmospheric DFe addition throughout the region, this group
539 constitutes only ~1% of total phytoplankton biomass.

540 Such differences in species response to external iron addition arise from differences in nutrient uptake between
541 different phytoplankton functional groups in CESM. Phytoplankton growth rate (μ_i) is parameterized as a product
542 of resource-unlimited growth rate (μ_{ref} in d^{-1}) at a reference temperature of 30°C, and three terms that describe
543 nutrient limitation (V_i), temperature dependence (T_f) and light availability (L_i). This is expressed as:

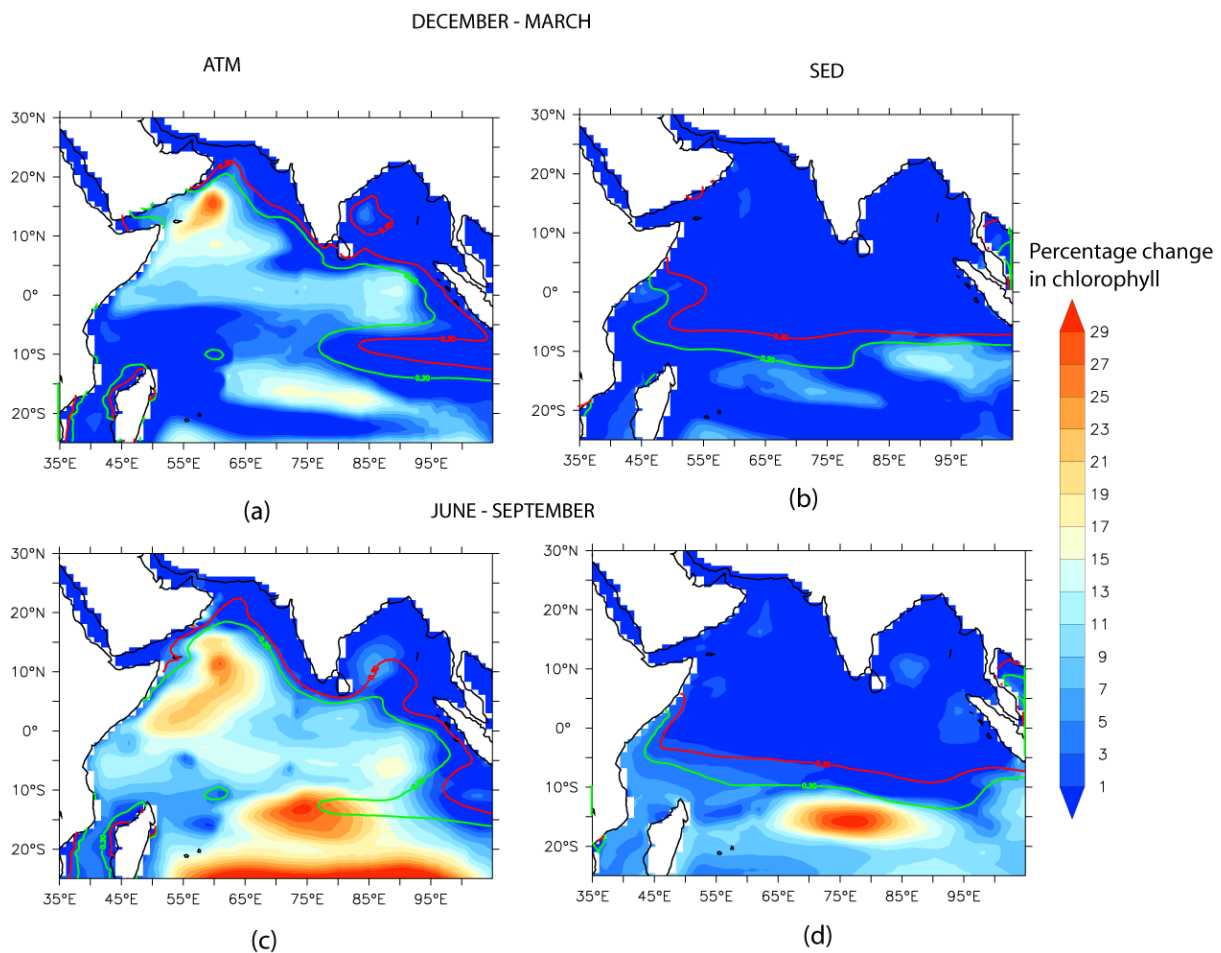
$$544 \mu_i = \mu_{ref} V_i T_f L_i \quad (1)$$

545 The nutrient limitation term for iron, V_i , for a specific phytoplankton group i is expressed as:

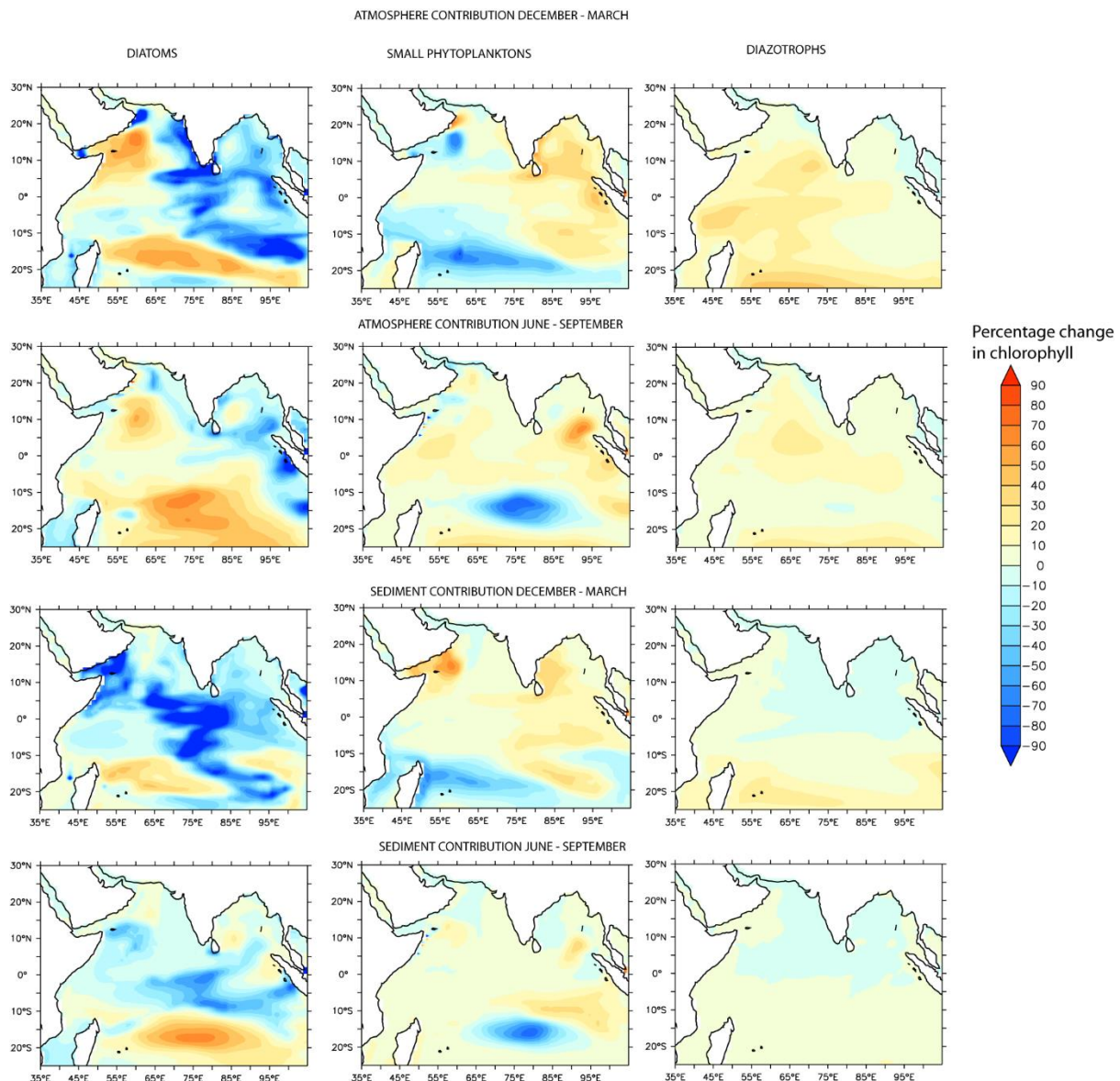
$$546 V_i^{Fe} = \frac{Fe}{Fe + K_i^{Fe}} \quad (2)$$

547 where Fe is the concentration of iron and K_i^{Fe} is the Fe uptake half-saturation constant for a phytoplankton group.
548 While small phytoplankton have been assigned a value of $3.0 \times 10^{-5} \text{ mmol m}^{-3}$ for K_i^{Fe} , diatoms have been
549 assigned a higher value of $7.0 \times 10^{-5} \text{ mmol m}^{-3}$. This leads to the small phytoplankton outcompeting diatoms when

550 nutrient levels are low. Additionally, small phytoplankton are subjected to higher grazing pressure than diatoms.
 551 The maximum grazing rate assigned in CESM is 3.3 d^{-1} for small phytoplankton versus 3.15 d^{-1} for diatoms.
 552 Together, the differences in nutrient uptake half-saturation constant and grazing pressure between different
 553 phytoplankton species results in diatom dominating blooms under nutrient-replete conditions.
 554 Diatoms outperforming other phytoplankton species has been previously witnessed in *in situ* iron fertilization
 555 experiments along with the existence of a linear relationship between diatom size and iron requirement for growth
 556 (de Baar et al., 2005). Such shifts in phytoplankton community structure in response to DFe additions are also
 557 corroborated by *in situ* experiments over the northern IO. For example, a nutrient addition experiment over the
 558 northern AS during northeast monsoon period has shown that the maximum positive phytoplankton response takes
 559 place due to nitrate+DFe addition (instead of only DFe addition), accompanied by around four-fold increases in
 560 coccolithophores, pennate and large centric diatoms (Takeda et al., 1995). Ship-board iron addition experiments
 561 over the AS during the southwest monsoon resulted in proliferation of visible colonies of haptophyte *Phaeocystis*
 562 *sp.* due to silicate-limitation (Moffett et al., 2015). Over the eastern IO, where both macronutrients and
 563 micronutrients are low, nutrient spiking with nitrogen, phosphorus, and iron resulted in increase of
 564 Prochlorococcus, Synechococcus, as well as Eukaryotes (Twining et al., 2019).
 565



566
 567 **Figure 5: Percentage contribution of (a and c) atmospheric and (b and d) sedimentary sources of iron during (a and b)**
 568 **the northeast monsoon and (c and d) the southwest monsoon to upper 100 m chlorophyll concentrations. Green and**
 569 **red contours show background DFe concentrations of 0.2 nM and 0.3 nM respectively. For the ATM (SED) case,**
 570 **background DFe is obtained from NATM (NSED) simulation.**
 571



572
 573 **Figure 6: Species-wise percentage contribution to column chlorophyll (0-100 m) response associated with atmospheric**
 574 **and sedimentary sources of DFe.**

575
 576
 577 **3.3.2 Responses to sedimentary sources of iron**

578 As shown in Fig. 4, sedimentary sources supply less than ~20% of DFe north of ~10°S latitude, whereas between
 579 10°-15°S latitude sedimentary iron can contribute to almost half of the total DFe concentrations. Unlike
 580 atmospheric sources, sedimentary supply of DFe is mostly confined to regions adjoining continental shelves and
 581 islands from where they are introduced to the open ocean by seasonally varying currents. In general, sedimentary
 582 sources make modest contribution to column productivity (<1% of chlorophyll anomalies) to the north of ~10°S
 583 latitude as described above. This is because high dust deposition to the north of the intertropical convergence zone
 584 results in high background DFe concentrations and controls productivity (see also Section 3.3.3). Sedimentary
 585 sources trigger the strongest positive phytoplankton response over the southern tropical IO region during June-
 586 September, where sedimentary DFe advected by the South Equatorial Current can facilitate more than 20%
 587 increase of the upper 100 m chlorophyll concentrations and ~40% increase at the surface. As noted in Section 3.2,

588 although atmospheric deposition contributes nearly half of the total DFe addition to this region, the total iron
589 deposition here is low (<0.2 nM). The phytoplankton response over the southern tropical IO is dominated by an
590 increase in diatoms, which contribute to more than 60% of total phytoplankton biomass (Fig. 6). In contrast, over
591 the regions experiencing $<1\%$ chlorophyll increase, there is a shift from diatoms towards small phytoplankton
592 species (Fig. 6). For example, there is more than 80% reduction in diatoms and 50% increase in small
593 phytoplankton over the western AS. Other current systems such as the poleward flowing Somali current, the
594 eastward flowing Southwest Monsoon Current and its southward extension along the west coast of Indonesia also
595 transport sedimentary DFe to the open ocean, but such advection supports only $\sim 5\%$ phytoplankton biomass.

596 It is important to mention here that DFe bias arising from source strength has low impact on phytoplankton
597 response to a particular source of DFe. This is because the strongest phytoplankton response to a specific DFe
598 source is over the western AS and subtropical southern IO. As noted in Section 3.1, these regions have the least
599 magnitude of DFe bias. For example, averaging over the upper 100 m over the northern IO, atmospheric source
600 contributes $\sim 13\%$ to total chlorophyll concentration. Even after masking out the region to the east of 65°E
601 longitude over the AS, where the highest positive DFe bias arising from atmospheric Fe has been noted, it is seen
602 that atmospheric source contributes $\sim 13\%$ to the upper 100 m chlorophyll concentration. Similarly, sedimentary
603 sources contribute $\sim 9\%$ to the upper 100 m chlorophyll concentration over the entire northern IO domain. Masking
604 out BoB, where DFe bias is due to enhanced sediment transport, results in sedimentary source contributing $\sim 8\%$
605 to the upper ocean chlorophyll concentration.

606

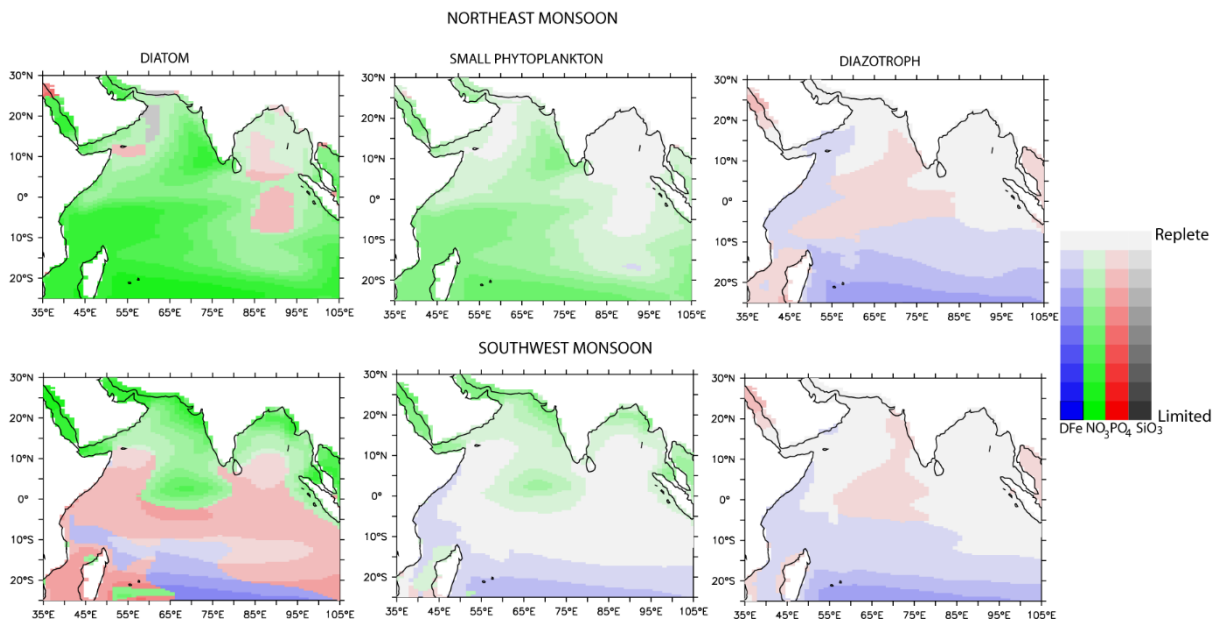
607 **3.3.3 Role of background nutrients in phytoplankton responses to external iron**

608

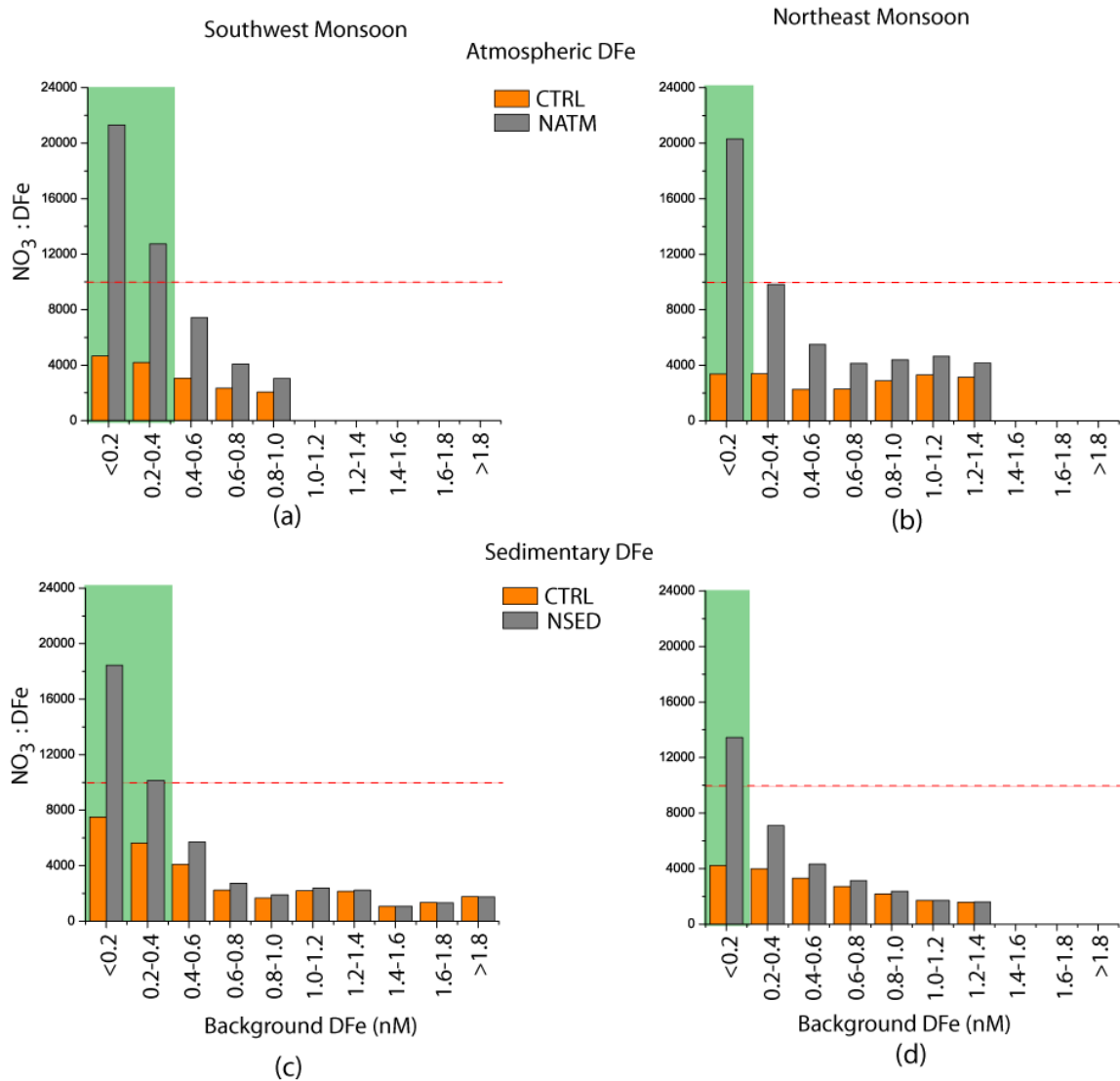
609 It emerges from the previous sections that there is heterogeneity in the phytoplankton response to atmospheric
610 and sedimentary sources of DFe. The regions of highest DFe input from a specific source are not always the
611 regions where strongest phytoplankton responses are evoked. What explains these differing patterns of
612 phytoplankton response? To examine this, patterns of nutrient limitations and iron supply from an external source
613 with respect to background DFe and nitrate (NO_3) concentrations are examined. In considering the phytoplankton
614 response to atmospheric sources (ATM case), background DFe is taken from the simulation without any
615 atmospheric source (NATM). Since river and hydrothermal sources make negligible contributions to DFe over
616 this domain, high levels of DFe in NATM mainly arise in regions where sedimentary sources are important.
617 Similarly, for estimating phytoplankton response to sedimentary sources (SED case), background DFe is taken
618 from simulation without any sedimentary source (NSED).

619 Generally, those regions experiencing greater than 1% increase in chlorophyll in response to atmospheric
620 (sedimentary) sources coincide with background DFe concentration <0.2 - 0.3 nM and high background NO_3 :DFe
621 ratio from the NATM (NSED) simulation. For example, in NATM simulation, iron serves as the dominant nutrient
622 that limits productivity over the entire northern IO, with diatoms experiencing stronger iron limitation compared
623 to other phytoplankton groups (Fig. S10). Iron limitation is particularly severe over central and southern AS,
624 equatorial IO and the southern tropical IO. In NSED case, there is a switch from nitrate limitation to the north of
625 the intertropical convergence zone to iron limitation to the south of the intertropical convergence zone (Fig. S11).
626 While iron stress is alleviated with addition of external DFe, there is a shift towards macronutrient, especially

627 nitrate, limitation (Fig. 7). South of $\sim 15^{\circ}\text{S}$ latitude continues to experience iron limitation during June-September
 628 due to very low dust deposition. In contrast, regions where chlorophyll increase is $<1\%$ following DFe addition
 629 are characterized by nitrate limitation in NATM/NSED simulations and external DFe cannot alleviate this primary
 630 nutrient limitation. This is further illustrated in Fig. 8 where upper ocean $\text{NO}_3:\text{DFe}$ ratio is plotted against
 631 background DFe concentrations. Positive chlorophyll response is elicited in regions of lowest background DFe
 632 and highest background $\text{NO}_3:\text{DFe}$ ratio. Over the world oceans, a wide range of cellular Fe:C ratios has been
 633 observed for diatoms, ranging from $100 \mu\text{mol mol}^{-1}$ for DFe-replete conditions (Twining et al., 2015; 2021) to 2
 634 $\mu\text{mol mol}^{-1}$ for DFe-deplete conditions (de Baar et al., 2008). Assuming a C:N ratio of 117:16 (Anderson and
 635 Sarmiento, 1994), the range of N:Fe ratios obtained are ~ 1000 and ~ 68000 , respectively, for DFe-replete and DFe-
 636 deplete conditions. Similarly, by considering iron limitation taking place for Fe:C ratio of $10 \mu\text{mol mol}^{-1}$ for open
 637 ocean species based on laboratory experiments (Sunda & Huntsman, 1995) and C:N ratio of 106:16, Measures
 638 and Vink (1999) have estimated that iron limitation over the AS water takes place at $\text{NO}_3:\text{DFe}$ ratio greater than
 639 ~ 15000 . In CESM simulations $>1\%$ increase in chlorophyll takes place when initial upper ocean $\text{NO}_3:\text{DFe}$ ratio
 640 is more than 10,000 corresponding to Fe-limitation scenario (Fig. 8). With the addition of DFe from atmospheric
 641 or sedimentary sources, the upper ocean $\text{NO}_3:\text{DFe}$ ratio reduces to less than 4000 in some cases, thereby leading
 642 to N-limitation. Previously, iron addition experiments in AS during the southwest monsoon have shown that the
 643 positive chlorophyll response depends on initial nitrate concentrations, with this response increasing in magnitude
 644 with higher initial nitrate concentrations (Moffett et al., 2015). In summary, the initial upper ocean $\text{NO}_3:\text{DFe}$ ratio
 645 sets the ultimate limit to the magnitude and distribution of phytoplankton response following external DFe
 646 additions.
 647



648
 649
 650 **Figure 7: Patterns of surface nutrient limitations for different phytoplankton functional types from CTRL simulation.**
 651 **Green: nitrate; blue: iron; red: phosphate; grey: silicate limitations.**
 652



653

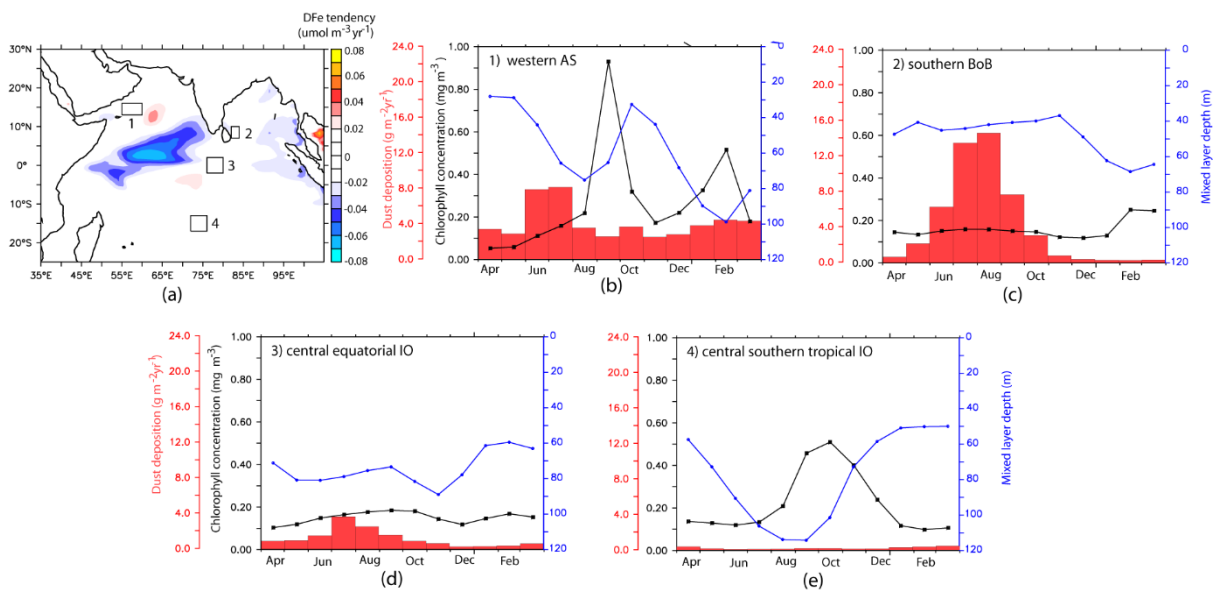
654 **Figure 8: Relation between background nutrients and phytoplankton response for atmospheric (a and b) and**
 655 **sedimentary (c and d) sources of DFe during (a and c) southwest monsoon and (b and d) northeast monsoon. The**
 656 **horizontal axis shows background DFe concentrations. The orange columns show upper ocean $\text{NO}_3 : \text{DFe}$ ratio for**
 657 **CTRL case and grey columns show $\text{NO}_3 : \text{DFe}$ ratio for (a-b) NATM and (c-d) NSED cases. The red dashed lines show**
 658 **the location where $\text{NO}_3 : \text{DFe}$ ratio is 10,000: below this value N-limitation prevails in CESM. Green shades highlight**
 659 **the regions where >1% increase in chlorophyll following DFe addition from a specific source is induced.**
 660

661 To sum up, atmospheric deposition is the most important source of DFe to the upper 100 m over the entire northern
 662 IO, followed by sedimentary sources. While atmospheric DFe is deposited over wide areas of the open ocean,
 663 sedimentary DFe fluxes arise only from continental shelves and are transported to open oceans through advection
 664 by currents. River and hydrothermal sources make negligible contributions to the total iron budget in the upper
 665 100 m. The primary response to atmospheric DFe is an increase in column-integrated phytoplankton biomass over
 666 most of the northern IO. In contrast, sedimentary source of iron is responsible for increases in column-integrated
 667 phytoplankton biomass mainly to the south of the intertropical convergence zone, where dust depositions are low.
 668 In general, significant positive responses of phytoplankton to addition of DFe are simulated only where low levels
 669 of background DFe concentrations and high values of background $\text{NO}_3 : \text{DFe}$ ratio are present. Otherwise, nitrate
 670 becomes the limiting nutrient once DFe is added. The simulations also show that positive chlorophyll response

671 to addition of DFe generally involves proliferation of diatoms, except over the equatorial IO where small
 672 phytoplankton increase is seen.

673
 674 **3.4 Iron budgets across different bio-physical regimes**

675 This section explores the main processes controlling DFe budget with respect to the role of atmospheric and
 676 sedimentary sources over different bio-physical regimes of the northern IO: (1) the western AS, (2) the southern
 677 BoB, (3) the central equatorial IO and (4) the central southern tropical IO. These regions encompass a wide range
 678 of productivity, with the first region being highly productive with OC-CCI chlorophyll exceeding 1.5 mg m^{-3} . The
 679 southern BoB and central southern tropical IO are moderately productive. Lastly, the central equatorial IO is
 680 oligotrophic with surface chlorophyll concentration being $\sim 0.1 \text{ mg m}^{-3}$. The locations of these regions along with
 681 CESM simulated seasonal cycles of mixed layer depths, chlorophyll and dust depositions are shown in Fig. 9.



682
 683 **Figure 9: (a) Net DFe tendency averaged over the upper 100 m for the study period. The boxes indicate the regions**
 684 **chosen for further studying DFe budget in Section 3.4. (b-e) Seasonal cycle of dust deposition (red columns), mixed**
 685 **layer depth (blue curves) and chlorophyll concentrations (black curves) from CESM-CTRL case for the four regions**
 686 **marked in (a).**

687
 688 The net dissolved iron tendency ($TEND_{DFe}$) is calculated as:

$$TEND_{DFe} = EXT + ADV + MIX + BIO \quad (3)$$

689
 690 where the source terms on the right describe dust/sediments/rivers/vents (EXT), horizontal and vertical advection
 691 (ADV), horizontal and vertical mixing (MIX) and biological sources/sinks (BIO). Advection includes explicitly
 692 resolved velocity as well as an additional “bolus” velocity from parameterization of mesoscale eddies (Gent &
 693 McWilliams, 1990). Vertical mixing includes a tracer gradient dependent term for cross-isopycnal mixing and a
 694 non-local mixing term, which accounts for mixing due to convective and shear instabilities (Large et al., 1994).
 695 Lateral mixing involves parameterization of mesoscale eddy-induced horizontal diffusion along isopycnal
 696 surfaces (Redi, 1982). The BIO term includes DFe losses due to biological iron uptake and scavenging, recycling

697 of iron back to the pool via remineralization, and iron released from phytoplankton and zooplankton losses and
698 grazing.

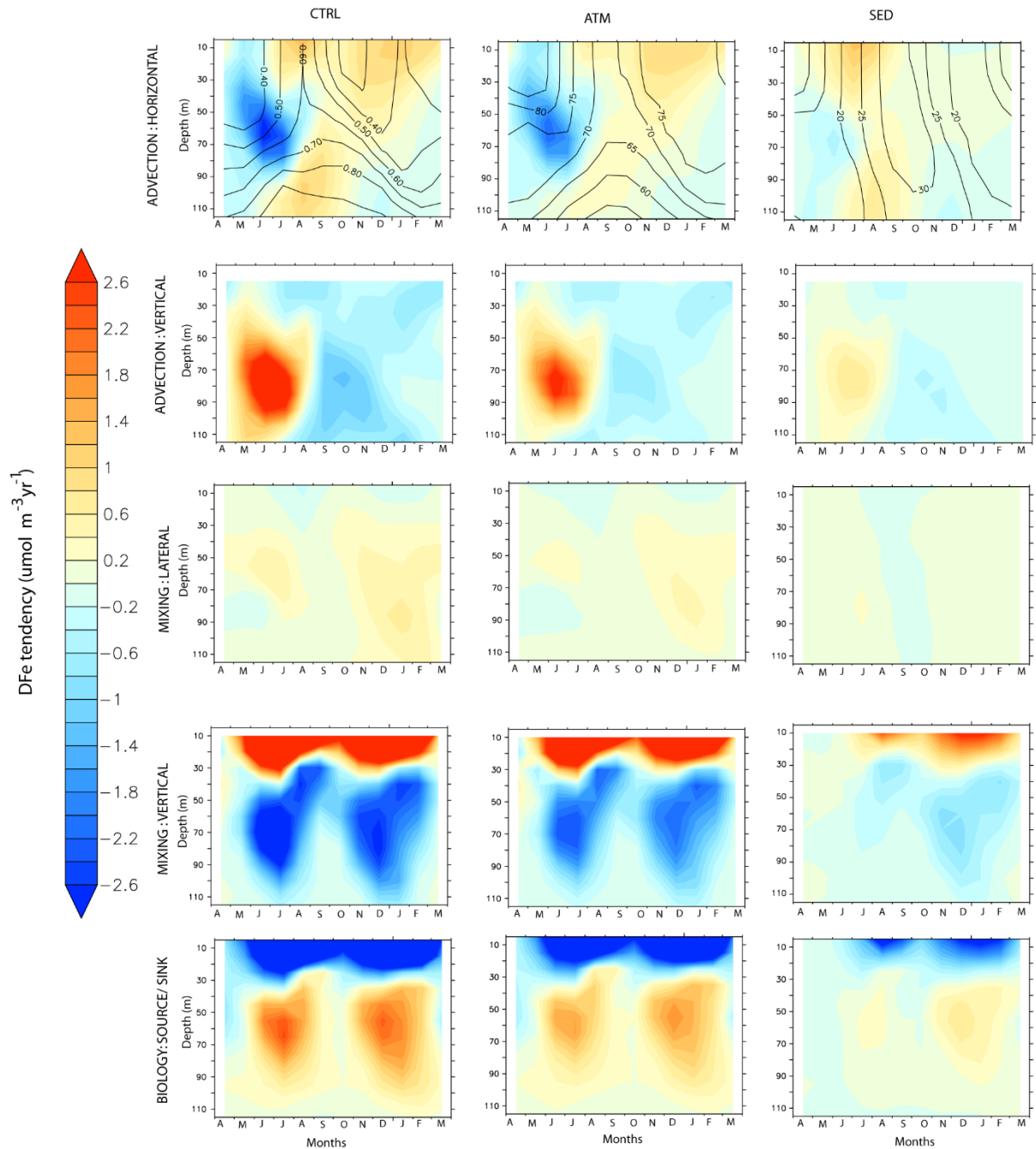
699 3.4.1 Western Arabian Sea

700 The western AS, off Oman and Yemen coastlines (considered here as 13°-16°N and 55°-60°E), is the most
701 productive region in the northern IO. Primary productivity in the western AS is highest during southwest monsoon
702 (Fig. 9b), during which alongshore southwesterly winds lead to upwelling and bring subsurface nutrients from
703 depths of ~150-200 m (Morrison et al., 1998). Some of this upwelled water advects eastwards, transporting
704 nutrients that enhance productivity in the central AS (Prasanna Kumar et al., 2001). The region also experiences
705 a secondary bloom during northeast monsoon due to winter convection that deepens the mixed layer. Integrated
706 over depths of the euphotic zone, average primary productivity over the western AS during mid and late southwest
707 monsoon is estimated at $135 \pm 10 \text{ mmol C m}^{-2} \text{ d}^{-1}$ and $110 \pm 11 \text{ mmol C m}^{-2} \text{ d}^{-1}$ respectively (Barber et al., 2001). In
708 comparison, primary productivity over the western AS during mid and late northeast monsoon is $137 \pm 13 \text{ mmol}$
709 $\text{C m}^{-2} \text{ d}^{-1}$ and $88 \pm 4 \text{ mmol C m}^{-2} \text{ d}^{-1}$ (Barber et al., 2001). Although this region encounters high dust deposition
710 (Haake et al., 1993; Mahowald et al., 2009), *in situ* measurements have hypothesized possible iron limitation
711 during late southwest monsoon because upwelled water is drawn from above the iron-rich sub-oxic zone (Naqvi
712 et al., 2010).

713 The largest peak in dust deposition is during southwest monsoon, followed by a second peak during northeast
714 monsoon (Fig. 9b). Accordingly, the upper ocean DFe concentration is highest during southwest monsoon and is
715 dominated by atmospheric sources (Fig. 10). Sedimentary contribution, although much lower, peaks during late
716 southwest monsoon and fall intermonsoon months. Throughout the year DFe concentration increases with depth,
717 thus pointing to consumption by phytoplankton at the surface. Vertical advection and vertical mixing are the most
718 important physical mechanisms governing DFe supply within this region during southwest monsoon (Fig. 10).
719 These processes begin to strengthen from May onwards to reach their peak during June-July and decrease
720 thereafter. Decomposing DFe advection tendency into tendencies arising from gradients in tracer distribution
721 ($D\text{Fe}'$) and velocity convergence (U') respectively, it is seen that vertical advection of DFe arises from $D\text{Fe}'$ and
722 U' in equal magnitude. However, the former process is dominant in June and the latter process dominates during
723 July (Fig. S12). The maximum vertical advection of DFe is centered around 80 m depth and progressively reduces
724 at shallower depths, as the vertical velocity reduces towards the surface. Vertical mixing prevailing in the upper
725 40 m brings this vertically advected DFe from subsurface to the surface. Furthermore, horizontal advection plays
726 an important role in redistributing this DFe supplied by vertical processes, with contributions from horizontal U'
727 being at least twice as large as $D\text{Fe}'$. During spring and early southwest monsoon, northeastward horizontal
728 advection removes atmospheric deposited DFe throughout the upper 100 m, while aiding the supply of
729 sedimentary DFe from Somalia and Omani continental shelves to the western AS. Later in the year as the
730 southwest monsoon current circulation is established, and meridional currents along the western AS become
731 stronger, its effect is first evident in the south along the Somali coast and progresses northward with time. The
732 result is convergence of both atmospheric and sedimentary DFe in the western AS during July-September. During
733 northeast monsoon, vertical mixing driven by winter convection, with the mixed layer deepening to 100 m, is the
734 most important means of DFe supply, from both atmospheric and sedimentary sources, into the surface layer.

735 Additionally, horizontal advection by westward currents transports DFe from atmospheric deposition in the central
736 AS into the western AS.

737 Removal of DFe from the water column is mainly through biological uptake in the upper 40 m. Uptake of DFe by
738 small phytoplankton dominate biological uptake throughout the year, except during September-October when
739 diatoms uptake of DFe becomes significant (not shown). This signature of diatoms is also observed in opal fluxes
740 measured by sedimentary traps deployed near the western AS and has been attributed to lowering of zooplankton
741 grazing pressures during late southwest monsoon (Smith, 2001) as well as to silicate limitation of diatoms in
742 initially upwelled waters (Haake et al., 1993). In the subsurface layer, remineralization of sinking fluxes of
743 particulate iron peaking at ~50 m replenishes the DFe pool during the latter part of the productive months (Fig.
744 S16a). Iron so released is made available to the surface layer via mixing or advection, thereby playing an important
745 role in maintaining surface DFe pool. Some of the remineralized DFe is further removed by scavenging, which
746 peaks at ~80 m during the productive months due to large fluxes of sinking particulate organic carbon, biogenic
747 silica, calcium carbonate and dust (Fig. S16a). Atmospheric deposition dominates biological source/sink of DFe
748 throughout the year, while sedimentary DFe is more important for biology during northeast monsoon months.



749
 750 **Figure 10: Evolution of the various terms of DFe budget, expressed as $\mu\text{mol m}^{-3} \text{yr}^{-1}$, by month and depth over the**
 751 **western Arabian Sea. Left panels: CTRL, Middle panels: ATM and, Right panels: SED case. The contours in the upper**
 752 **panel for CTRL show evolution of DFe concentrations (nM), while the contours in the upper panels for ATM and SED**
 753 **cases show the percentage contribution of each of these cases to total DFe concentrations in CTRL case.**

754

755 3.4.2 Southern Bay of Bengal

756 The region corresponding to the southern BoB (7° - 10° N and 82° - 84° E) is located to the east of Sri Lanka.
 757 Compared to the rest of the BoB, freshwater flux from South Asian rivers reduces markedly in this region due to
 758 advection of high salinity water from AS by the eastward flowing Southwest Monsoon Current (see Fig. 2h) as
 759 well as upward pumping of saltier water by thermocline doming during the southwest monsoon season
 760 (Vinayachandran et al., 2013). This leads to stronger biophysical coupling in the southern BoB, compared to the
 761 rest of the bay, through erosion of the upper stable layer of freshwater capping. During southwest monsoon, the

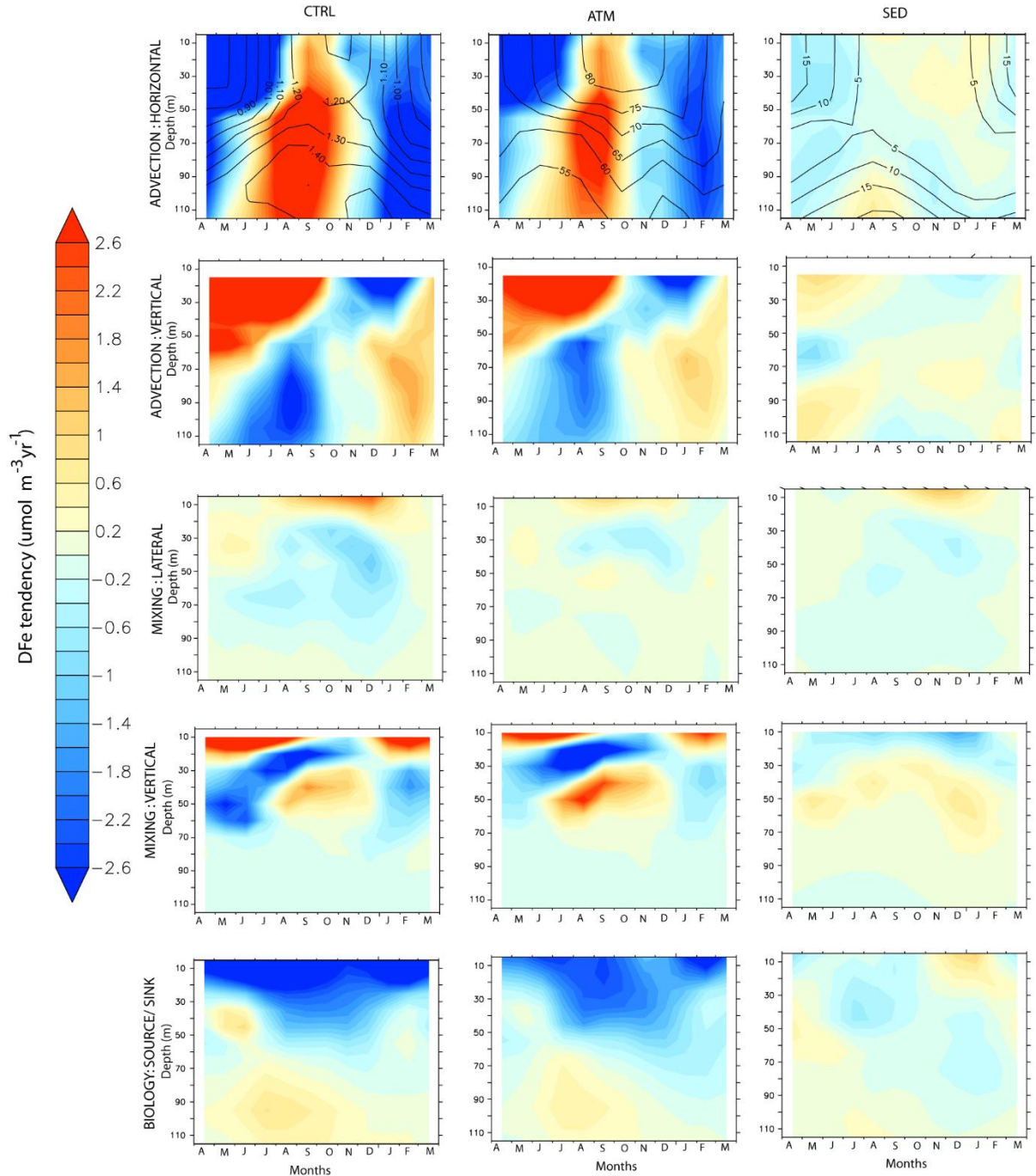
762 Southwest Monsoon Current advects nutrients and chlorophyll from the upwelling regions along the southern tip
763 of India and Sri Lanka into the southern BoB (Vinayachandran et al., 2004). Over the open southern BoB, to the
764 east of Sri Lanka, cyclonic wind stress curl drives open ocean upwelling leading to shoaling of the thermocline
765 that forms the Sri Lankan dome. This results in surface chlorophyll concentration between 0.3-0.7 mg m⁻³ and
766 strong subsurface chlorophyll maxima between 20-50 m where chlorophyll concentration can exceed 1 mg m⁻³
767 (Thushara et al., 2019). A much lower magnitude of surface chlorophyll concentration (~0.18 mg m⁻³, Fig. 9c)
768 and subsurface chlorophyll maxima (~0.2 mg m⁻³) at 40-60 m depth is simulated by CESM. During the northeast
769 monsoon, CESM simulates a second bloom over this region associated with winter cooling and mixed layer
770 deepening to ~60 m (Fig. 9c). This bloom has slightly higher magnitude, peaking at ~0.25 mg m⁻³, compared to
771 the southwest monsoon bloom. Surface chlorophyll data from OC-CCI also reveals the presence of northeast
772 monsoon blooms (peak at ~0.25 mg m⁻³), which during some years are of higher magnitude than southwest
773 monsoon blooms. Argo data in this region also show signatures of mixed layer deepening during winter (not
774 shown).

775 Overall, the highest DFe over this region is encountered during the late southwest monsoon and is dominated by
776 atmospheric deposition (Fig. 11). Vertical advection is the most important process supplying DFe to the surface
777 layers during spring and southwest monsoon months (Fig. 11). This is aided by a positive wind stress curl
778 established over the region from March onwards. While vertical velocity is positive during the southwest monsoon
779 over the entire depth considered, DFe supply by vertical advection is positive only for depths less than 50 m (Fig.
780 S13). This is because the magnitude of upward velocity gradually reduces with depth, resulting in positive values
781 of U' upwards from 40 m depths. (Fig. S13). With the arrival of westward propagating Rossby waves to the
782 western boundary of the BoB during October, upwelling favorable vertical motion collapses (Webber et al., 2018).

783 With respect to horizontal advection, it is seen that the magnitude and sign of convergence by the meridional
784 component of the current mainly controls DFe supply over the southern BoB. This arises from the southward
785 flowing current to the western flank of the Sri Lankan dome that supplies atmospheric DFe to this region. This
786 DFe supplied by the southwards current, as well as DFe derived from upwelling, is removed by the energetic
787 eastward currents during late spring to early fall intermonsoon months. During the rest of the year, the westward
788 flowing currents supplies some sedimentary DFe from the Andaman Sea to the southern BoB. However, the much
789 larger magnitude of dust deposition in the north-western BoB leads to overall negative tracer gradients and, thus,
790 dilution of DFe by horizontal advection. The most important DFe supply mechanism during northeast monsoon
791 is enhanced vertical mixing in the upper 20 m associated with deepening of mixed layer. Additionally,
792 downwelling due to weakly negative wind stress curl during this time of the year removes DFe from the surface
793 and favors its accumulation in the subsurface ocean. Lateral mixing complements DFe supply to the upper 20 m
794 during fall and early northeast monsoon, especially from sedimentary sources.

795 Biological uptake removes DFe throughout the year from the upper 40 m especially during the southwest and
796 northeast monsoon blooms (Fig. 11). DFe uptake in the upper 40 m is dominated by small phytoplankton during
797 most of the year, except during northeast monsoon (not shown). Diatom DFe uptake, on the other hand, dominates
798 the deep chlorophyll maxima present between 40-70 m throughout the year as well as within the surface layer
799 during northeast monsoon months. Several studies have pointed to substantial nutrient uptake by diatoms in the
800 central, coastal, and northern BoB due to riverine supply of silicates (Madhu et al., 2006; Madhupratap et al.,

801 2003). Remineralization of particulate iron as well as iron release from grazing and mortality of phytoplankton
 802 and zooplankton have a primary peak between 50 m-80 m during July-August and secondary peak during
 803 February-March. On the contrary, scavenging removes DFe, with its effect peaking during July-August during
 804 blooms (Fig. S16b).



805
 806 **Figure 11: Same as Figure 10, except over the southern Bay of Bengal.**

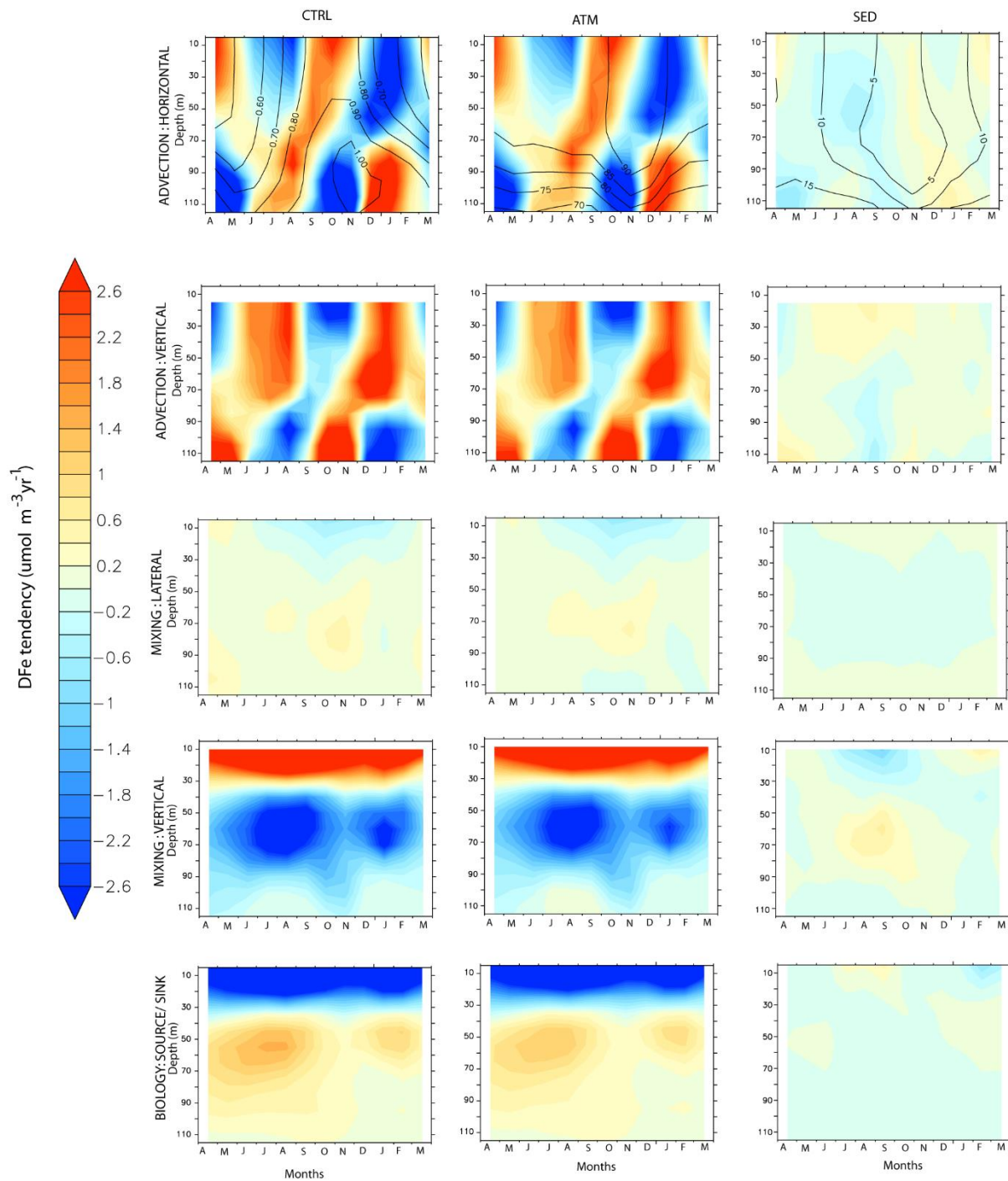
807
 808 **3.4.3 Central Equatorial IO**

809 With chlorophyll concentrations around 0.1 mg m^{-3} for most part of the year, the central equatorial IO (2°S - 2°N
 810 and 76° - 80°E) is the least productive of all the regions considered (Fig. 9d). Unlike its counterparts in the Pacific

811 and the Atlantic Oceans, the equatorial IO experiences only transient upwelling due to changes in wind direction
812 associated with migration of the intertropical convergence zone. This also leads to surface currents reversing their
813 direction four times a year. Thus, the region experiences westward surface currents of weak magnitude during the
814 southwest and northeast monsoon months and much stronger eastwards current during the spring and fall
815 intermonsoon months (Han et al., 1999). These narrow eastwards surface currents during the intermonsoon
816 months, known as Wyrтки jets, are in response to westerly winds (Wyrтки, 1973). The biogeochemical
817 characteristics of the region have only been recently explored with the help of satellite and *in situ* data (e.g.,
818 Prasanna Kumar et al., 2012; Strutton et al., 2015). Deepening of the surface layer associated with the eastward
819 transport of water during the intermonsoon months lowers productivity (Prasanna Kumar et al., 2012).
820 Chlorophyll concentrations, although much lower compared to the rest of the IO, peaks during October-December
821 possibly due to wind stirring or shear instability at the base of the eastward moving Wyrтки Jet (Strutton et al.,
822 2015). Additionally, *in situ* measurements in the central equatorial IO have revealed deep chlorophyll maxima
823 located ~60 m depth contributing to more than 30% of the total chlorophyll biomass (Vidya et al., 2013). The
824 peak ocean DFe concentration is encountered during August-November. Overall, comparison between CTRL,
825 ATM and SED cases show that atmospheric deposition, peaking during July (Fig. 9d), dominates DFe contribution
826 to the central equatorial IO, whereas sedimentary DFe plays a distant secondary role (Fig. 12).

827 Horizontal advection is the most important process of DFe supply within the mixed layer during March-May and
828 September-November (Fig. 12). During the intervening months, vertical advection plays the predominant role in
829 DFe supply. Decomposing the horizontal advection further into $D\text{Fe}'$ and U' reveals that the meridional velocity
830 convergence is the main contributor to the central equatorial IO DFe budget during March-May and September-
831 November (Fig. S14). This originates from the westerly wind directing equatorward Ekman flow in both the
832 hemispheres, which leads to convergence and drives eastward propagating downwelling Kelvin wave (McPhaden
833 et al., 2015). Averaged over the upper 100 m, zonal velocity convergence, although somewhat of lower magnitude,
834 opposes meridional velocity convergence throughout the year. When the Wyrтки jet weakens, upwelling induced
835 by easterly wind drives upward vertical supply of DFe, whereas there is downward vertical removal of DFe during
836 the intervening periods. This alternating between upwelling and downwelling control on DFe has an upward phase
837 propagation. An important feature of the central equatorial IO, in contrast to other equatorial regions, is the
838 presence of transient Equatorial Undercurrent between 60 m-200 m depth with core generally centered on the
839 depth of the 20°C isotherm (Chen et al., 2015). The Equatorial Undercurrent appears most strongly during winter-
840 spring months and with much weaker magnitude during summer-fall months (Chen et al., 2015; Schott &
841 McCreary, 2001). CESM simulation reveals the signature of the upper part of the Equatorial Undercurrent in
842 influencing DFe budget. This is characterized by the zonal velocity underneath the mixed layer (~80 m depth)
843 showing strong eastward transport during January-April and a much weaker eastward transport during September-
844 November. The horizontal convergence of DFe is prominent during the developing phase of the Equatorial
845 Undercurrent (December-February and June-August), probably, associated with progressive eastward extension
846 and strengthening of Equatorial Undercurrent from the western IO. These periods of horizontal DFe convergence
847 are interspersed with vertical DFe convergence. Superimposed on advection, vertical mixing plays an important
848 role in bringing subsurface DFe to the surface levels in the upper 30 m, peaking during July-August.

849 Biological removal of DFe, almost entirely by small phytoplankton, is conspicuous in the upper 40 m and peaks
850 during September. This is in line with sediment trap studies over the central equatorial IO where peak biogenic
851 fluxes are detected during the southwest and fall intermonsoon months and are dominated by coccolithophorids
852 and foraminifera carbonate (Ramaswamy and Gaye, 2006). Furthermore, *in situ* water samples have shown that
853 picoplankton, having size less than 10 μm , consists of more than 90% of the phytoplankton biomass in central
854 equatorial IO (Vidya et al., 2013). The period of peak biogenic flux is also characterized by peak in DFe removal
855 by scavenging and remineralization of particulate iron released from mortality and grazing at deeper layers (Fig.
856 S16c). A secondary increase in biological removal of DFe is noticed during January-March associated with a
857 secondary peak in chlorophyll, although its impact is not evident in sediment trap biogenic flux data (Vidya et al.,
858 2013). This might arise from remineralization of particulate iron being almost twice the magnitude of scavenging
859 losses during this time of the year.



860

861 **Figure 12: Same as Figure 10, except over the central equatorial Indian Ocean.**

862

863 3.4.4 Central Southern Tropical IO

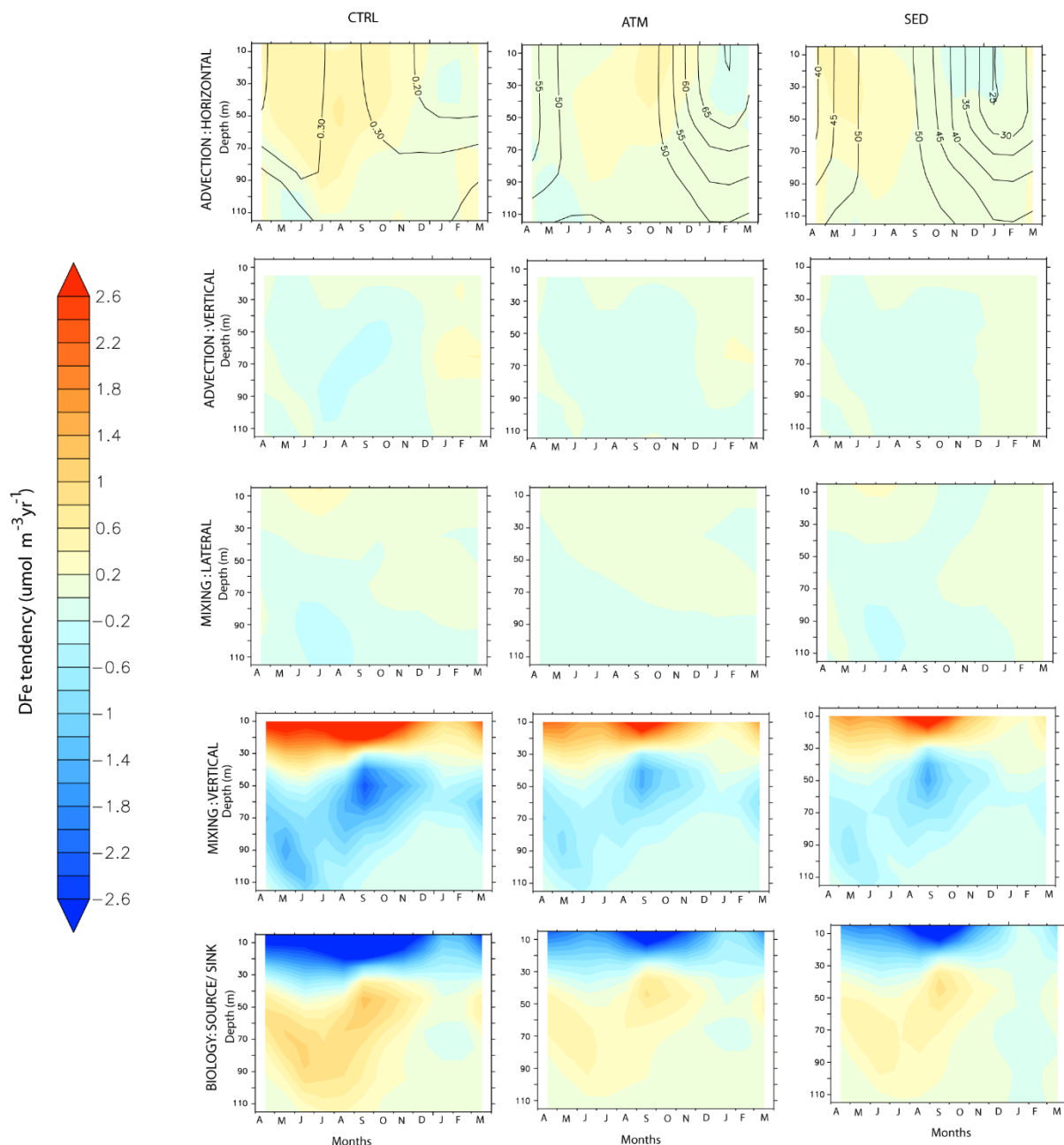
864 The central southern tropical IO (13°-17°S and 72°-76°E) is located in the transition zone between DFe-poor region
 865 of the subtropical IO gyre and DFe-enriched northern IO. Of all the regions considered, this receives the lowest
 866 atmospheric DFe (Fig. 9e), resulting in DFe limitation of phytoplankton growth particularly during the boreal
 867 summer (Fig. 7). Steady southeasterly winds, prevailing throughout the year, transport dust from Australian
 868 sources into this region. Peak in dust deposition is during austral spring and summer associated with strong source

869 activity (Kok et al., 2021; Yang et al., 2021). A secondary peak in dust deposition during austral winter is possibly
870 associated with enhanced transport. Northern part of the central southern tropical IO lies on the Seychelles-Chagos
871 thermocline ridge, which is characterized by doming up of the thermocline due to negative wind stress curl
872 resulting in Ekman divergence (Vialard et al., 2009). The thermocline progressively deepens towards the sub-
873 tropical southern IO gyre to the south as wind stress curl changes sign to positive. The westward flowing South
874 Equatorial Current brings low salinity water and nutrients from the Indonesian region. Satellite observed enhanced
875 chlorophyll concentration during the boreal (austral) summer (winter) months have been attributed to vertical
876 diffusion (Košić et al., 2009; Lévy et al., 2007). Additionally, westward propagating upwelling/downwelling
877 Rossby waves arrive in this region following La Nina/El Nino event and play a key role in modulating sea surface
878 height and the depth of thermocline (Masumoto & Meyers, 1998; Périgaud & Delecluse, 1992). This perturbs the
879 depth of nitracline, which has significant impact on column productivity (Kawamiya & Oschlies, 2001).

880 Both ATM and SED sources are important in this region for DFe supply, with the SED (ATM) source having
881 higher contribution during austral winter (summer) months (Fig. 13). Analysis of CESM-simulated DFe budget
882 reveals that vertical mixing in the upper 30 m is the most important process of DFe supply, which peaks during
883 September. This is the time of the year when CESM records the lowest sea surface temperature resulting in mixed
884 layer deepening. Such winter mixing leads to erosion of vertical gradient in DFe observed during the rest of the
885 year in the upper 120 m. Horizontal advection is the next most important supplier of DFe in this region. The
886 westward flowing South Equatorial Current is strongest during austral winter and during winter-to-summer
887 transition months. This results in meridional velocity convergence and zonal velocity divergence resulting in a
888 quasi-balance between DFe supply and removal (Fig. S15). Overall, horizontal advection leads to predominantly
889 sedimentary DFe convergence during March-June and predominantly atmospheric DFe convergence during
890 September-November.

891 The wind stress curl is mostly negative, that is upwelling favorable, throughout the year. Between April-October
892 (austral winter), when winter convection-driven blooms are prominent, wind stress curl becomes weakly negative
893 to slightly positive. Following this, during January-March, the wind stress curl becomes strongly negative
894 resulting in upward velocity and favors vertical advection of both atmospheric and sedimentary DFe in equal
895 magnitude. While vertical U' is responsible for supplying DFe in the upper 50 m, vertical DFe' is important at
896 deeper depths (Fig. S15).

897 The biological sink of DFe peaks during the month of maximum vertical mixing, that is, during September.
898 During this time, uptake of DFe is dominated by diatoms, which accounts for more than 80% of the total DFe
899 uptake. Small phytoplankton dominate the rest of the year. Scavenging removal of DFe and particulate iron
900 remineralization peaks one month later during October between 50-90 m depth range (Fig. S16d). Overall, the
901 central southern tropical IO is the only region where atmospheric deposition and sedimentary sources of iron are
902 equally important in driving the DFe budget.



903

904 **Figure 13: Same as Figure 10, except over the central southern tropical Indian Ocean.**

905

906 **4 Conclusions**

907

908 Using the ocean component of the Earth system model CESM version 2.1, this study elucidates the impacts of
 909 various sources of DFe on upper ocean productivity, nutrient limitations and DFe budgets over the northern IO.
 910 The iron cycle in CESM represents the complex interplay between several processes including DFe supply,
 911 removal by scavenging and biological uptake, particulate iron remineralization, and organic ligand complexation.
 912 The major sources of DFe for this region are included in this model: atmospheric deposition, sediments,
 913 hydrothermal vents, and rivers. Although there are model biases in representing physical and biogeochemical
 914 variables, the overall patterns of spatial and temporal variation of DFe are simulated reasonably well in CESM.

915 The study finds that atmospheric deposition is the most important source of DFe to the northern IO. Atmospheric
916 deposition contributes well over 50% of the total DFe concentration and more than 10% (35%) to upper 100 m
917 (surface level) chlorophyll concentrations, especially over the AS, equatorial IO, and southern tropical IO.
918 Sedimentary sources become important along continental shelves, where they can contribute to more than 20% of
919 total DFe. The sedimentary source has the largest impact in fueling phytoplankton blooms over the southern
920 tropical IO during June-September. In contrast, hydrothermal and river sources have negligible impacts on upper
921 ocean DFe pools in this region. Almost all regions that experience significant positive chlorophyll responses to
922 atmospheric as well as sedimentary sources of DFe show a preponderance of diatoms over other phytoplankton
923 groups. The increases in phytoplankton following external DFe addition are evoked in regions with low
924 background DFe levels (<0.3 nM) and high initial NO₃:DFe, indicating the importance of high levels of
925 macronutrients. Following, external DFe addition, a shift to nitrate limitation of phytoplankton is observed.

926 Analysis of DFe budget across different biophysical regimes in the northern IO shows that this budget is generally
927 dominated by atmospheric deposition, with sedimentary sources of DFe being a distant second contributor. The
928 exception to this occurs over the southern tropical IO region, where both atmospheric and sedimentary sources
929 become equally important. In all the regions considered, vertical mixing is the most important physical mechanism
930 through which DFe is supplied, and furthermore this mechanism is active almost throughout the year. In contrast,
931 the importance of horizontal and vertical advection is highly seasonal. DFe uptake by small phytoplankton in the
932 upper ocean is the most important route through which DFe removal takes place, except in the productive waters
933 where diatoms also participate in the removal process. At subsurface levels, competition between the removal of
934 DFe by scavenging and remineralization of particulate iron determines the DFe pool available to the surface ocean
935 via these aforementioned physical processes.

936 Of all DFe sources, atmospheric deposition is most likely vulnerable to future global warming, and changes to it
937 will perhaps exert strong influence on upper ocean productivity and nutrient limitation. Additionally, 59% of the
938 continental shelves and bathyal sea floor over the northern IO experiences hypoxic conditions (Helly and Levin,
939 2004) and there are several lines of evidence pointing to reductions in oxygen content over this region during the
940 last few decades due to enhanced upper ocean stratification (Schmidtko et al., 2017). This will possibly impact
941 the flux of iron from reduced sediments. The present study thus provides foundations to explore how different
942 future scenarios of atmospheric deposition and the extent of reducing sediments can impact biogeochemistry over
943 the northern IO.

944

945 **Code and data availability**

946 Climatology of ocean temperature, salinity and nutrients are from World Ocean Atlas 2018 available at
947 <https://www.ncei.noaa.gov/access/world-ocean-atlas-2018/>. Monthly surface chlorophyll data from OC-CCI is
948 obtained from <https://www.oceancolour.org/>. Monthly climatology of ocean mixed layer depth based on Holte et
949 al. (2017) is downloaded from <http://mixedlayer.ucsd.edu/>. Surface ocean current data from OSCAR can be
950 downloaded from: [https://podaac.jpl.nasa.gov/dataset/OSCAR_L4_OC_third-](https://podaac.jpl.nasa.gov/dataset/OSCAR_L4_OC_third-deg?ids=Keywords:Keywords:Projects&values=Oceans::Solid%20Earth::OSCAR&provider=PODAAC)
951 [deg?ids=Keywords:Keywords:Projects&values=Oceans::Solid%20Earth::OSCAR&provider=PODAAC](https://podaac.jpl.nasa.gov/dataset/OSCAR_L4_OC_third-deg?ids=Keywords:Keywords:Projects&values=Oceans::Solid%20Earth::OSCAR&provider=PODAAC).

952 Dissolved iron from GEOTRACES Intermediate Data Product 2021 is available at
953 <https://www.geotraces.org/geotraces-intermediate-data-product-2021/>. Additionally, dissolved iron profile data

954 are also obtained from Tagliabue et al. (2012) available at <https://www.bodc.ac.uk/geotraces/data/historical/>. The
955 code for CESM2.1 can be downloaded from https://www.cesm.ucar.edu/models/cesm2/release_download.html
956 (last access: 01 December 2020).

957 **Author contributions**

958 PB conceived the study, carried out model simulations, analysed the data and wrote the manuscript.

959 **Competing interests**

960 The author declares that there is no conflict of interest.

961 **Acknowledgments**

962 PB acknowledges the computational facilities provided by Supercomputer Education and Research Centre
963 (SERC) at the Indian Institute of Science for carrying out CESM simulations. PB is also grateful to Anh Pham,
964 Nicola Wiseman, and an anonymous reviewer for the constructive comments, which have significantly improved
965 this manuscript.

966 **Financial support**

967 The author is supported by Department of Science and Technology INSPIRE Faculty scheme
968 (DST/INSPIRE/04/2018/002625).

969 **References**

970 Anand, S. S., Rengarajan, R., Sarma, V. V. S. S., Sudheer, A. K., Bhushan, R., and Singh, S. K.: Spatial variability
971 of upper ocean POC export in the Bay of Bengal and the Indian Ocean determined using particle-reactive ^{234}Th ,
972 *J. Geophys. Res.-Oceans*, 122, 3753–3770, <https://doi.org/10.1002/2016JC012639>, 2017.

973 Anand, S. S., Rengarajan, R., Shenoy, D., Gauns, M., and Naqvi, S. W. A.: POC export fluxes in the Arabian Sea
974 and the Bay of Bengal: A simultaneous ^{234}Th / ^{238}U and ^{210}Po / ^{210}Pb study, *Mar. Chem.*, 198, 70–87,
975 <https://doi.org/10.1016/j.marchem.2017.11.005>, 2018.

976 Anderson, L. and Sarmiento, J.: Redfield ratios of remineralization determined by nutrient data analysis, *Global*
977 *Biogeochem. Cy.*, 8, 65–80, <https://doi.org/10.1029/93GB03318>, 1994.

978 Armstrong, R. A., Lee, C., Hedges, J. I., Honjo, S., and Wakeham, S.: A new, mechanistic model for organic
979 carbon fluxes in the ocean: based on the quantitative association of POC with ballast minerals, *Deep-Sea Res.*,
980 49, 219–236, 2002.

981 Banerjee, P. and Kumar, S. P.: Dust-induced episodic phytoplankton blooms in the Arabian Sea during winter
982 monsoon, *J. Geophys. Res.-Oceans*, 119, 7123–7138,
983 <https://doi.org/10.1002/2014JC010304>, 2014.

984 Banerjee, P., Sathesh, S. K., Moorthy, K. K., Nanjundiah, R. S., and Nair, V. S.: Long-range transport of mineral
985 dust to the northeast Indian Ocean: Regional versus remote sources and the implications, *J. Clim.*, 32, 1525–1549,
986 <https://doi.org/10.1175/JCLI-D-18-0403.1>, 2019.

987 Barber, R. T., Marra, J., Bidigare, R. C., Codispoti, L. A., Halpern, D., Johnson, Z., Latasa, M., Goericke, R., and
988 Smith, S. L.: Primary productivity and its regulation in the Arabian Sea during 1995, *Deep-Sea. Res. Pt. II*, 48,
989 1127–1172, [https://doi.org/10.1016/S0967-0645\(00\)00134-X](https://doi.org/10.1016/S0967-0645(00)00134-X), 2001.

990 Beal, L. M., Field, A., and Gordon, A. L.: Spreading of Red Sea overflow waters in the Indian Ocean, *J. Geophys.*
991 *Res.*, 105, 8549–8564, <https://doi.org/10.1029/1999JC900306>, 2000.

992 Bianchi, D., Dunne, J. P., Sarmiento, J. L., and Galbraith, E. D.: Data-based estimates of suboxia, denitrification,
993 and N₂O production in the ocean and their sensitivities to dissolved O₂, *Global Biogeochem. Cy.*, 26, GB2009,
994 <https://doi.org/10.1029/2011gb004209>, 2012.

995 Blain, S., Quéguiner, B., Armand, L., Belviso, S., Bombled, B., Bopp, L., Bowie, A., Brunet, C., Brussaard, C.,
996 Carlotti, F., Christaki, U., Corbière, A., Durand, I., Ebersbach, F., Fuda, J.-L., Garcia, N., Gerringa, L., Griffiths,
997 B., Guigue, C., Guillermin, C., Jacquet, S., Jeandel, C., Laan, P., Lefèvre, D., Lo Monaco, C., Malits, A., Mosseri,
998 J., Obernosterer, I., Park, Y.-H., Picheral, M., Pondaven, P., Remenyi, T., Sandroni, V., Sarthou, G., Savoye, N.,
999 Scouarnec, L., Souhaut, M., Thuiller, D., Timmermans, K., Trull, T., Uitz, J., van Beek, P., Veldhuis, M., Vincent,
1000 D., Viollier, E., Vong, L., and Wagener, T.: Effect of natural iron fertilization on carbon sequestration in the
1001 Southern Ocean, *Nature*, 446, 1070–1074, <https://doi.org/10.1038/nature05700>, 2007.

1002 Boss, E. and Behrenfeld, M.: In situ evaluation of the initiation of the North Atlantic phytoplankton bloom,
1003 *Geophys. Res. Lett.*, 37, L18603, <https://doi.org/10.1029/2010GL044174>, 2010.

1004 Boyd, P. W. and Ellwood, M. J.: The biogeochemical cycle of iron in the ocean, *Nat. Geosci.*, 3, 675–682,
1005 <https://doi.org/10.1038/ngeo964>, 2010.

1006 Buck, K. N., Lohan, M. C., Berger, C. J., and Bruland, K. W.: Dissolved iron speciation in two distinct river
1007 plumes and an estuary: Implications for riverine iron supply, *Limnol. Oceanogr.*, 52, 843–855,
1008 <https://doi.org/10.4319/lo.2007.52.2.0843>, 2007.

1009 Buesseler, K., Ball, L., Andrews, J., Benitez-Nelson, C., Belostock, R., Chai, F., and Chao, Y.: Upper ocean export
1010 of particulate organic carbon in the Arabian Sea derived from thorium-234, *Deep-Sea Res. Pt. II*, 45, 2461–2487,
1011 [https://doi.org/10.1016/S0967-0645\(98\)80022-2](https://doi.org/10.1016/S0967-0645(98)80022-2), 1998.

1012 Canfield, D. E.: The geochemistry of river particulates from the continental USA: Major elements, *Geochim.*
1013 *Cosmochim. Ac.*, 61, 3349–3365, [https://doi.org/10.1016/s0016-7037\(97\)00172-5](https://doi.org/10.1016/s0016-7037(97)00172-5), 1997.

1014 Chen, G., Han, W., Li, Y., Wang, D., and McPhaden, M. J.: Seasonal-to-interannual time-scale dynamics of the
1015 equatorial undercurrent in the Indian Ocean, *J. Phys. Oceanogr.*, 45, 1532–1553, [https://doi.org/10.1175/JPO-D-](https://doi.org/10.1175/JPO-D-14-0225.1)
1016 14-0225.1, 2015.

1017 Chinni, V., Singh, S. K., Bhushan, R., Rengarajan, R., and Sarma, V. V. S. S.: Spatial variability in dissolved iron
1018 concentrations in the marginal and open waters of the Indian Ocean, *Marine Chem.*, 208, 11–28,
1019 <https://doi.org/10.1016/j.marchem.2018.11.007>, 2019.

- 1020 Chinni, V., and Singh, S. K.: Dissolved iron cycling in the Arabian Sea and sub-tropical gyre region of the Indian
1021 Ocean, *Geochim. Cosmochim. Ac.*, 317, 325-348, <https://doi.org/10.1016/j.gca.2021.10.026>, 2022.
- 1022 Conway, T. M. and John, S. G.: Quantification of dissolved iron sources to the North Atlantic Ocean, *Nature*, 511,
1023 212–215, <https://doi.org/10.1038/nature13482>, 2014.
- 1024 Dai, A., Qian, T., Trenberth, K. E., and Milliman, J. D.: Changes in continental freshwater discharge from 1948
1025 to 2004, *J. Climate*, 22, 2773–2792, <https://doi.org/10.1175/2008JCLI2592.1>, 2009.
- 1026 Danabasoglu, G., Bates, S. C., Briegleb, B. P., Jayne, S. R., Jochum, M., Large, W. G., Peacock, S., and Yeager,
1027 S. G.: The CCSM4 ocean component, *J. Climate*, 25, 1361–1389, <https://doi.org/10.1175/JCLI-D-11-00091.1>,
1028 2012.
- 1029 Danabasoglu, G., Lamarque, J.-F., Bacmeister, J., Bailey, D. A., DuVivier, A. K., Edwards, J., Emmons, L. K.,
1030 Fasullo, J., Garcia, R., Gettelman, A., Hannay, C., Holland, M. M., Large, W. G., Lauritzen, P. H., Lawrence, D.
1031 M., Lenaerts, J. T. M., Lindsay, K., Lipscomb, W. H., Mills, M. J., Neale, R., Oleson, K. W., Otto-Bliesner, B.,
1032 Phillips, A. S., Sacks, W., Tilmes, S., van Kampenhout, L., Vertenstein, M., Bertini, A., Dennis, J., Deser, C.,
1033 Fischer, C., Fox-Kemper, B., Kay, J. E., Kinnison, D., Kushner, P. J., Larson, V. E., Long, M. C., Mickelson, S.,
1034 Moore, J. K., Nienhouse, E., Polvani, L., Rasch, P. J., and Strand, W. G., The Community Earth System Model
1035 Version 2 (CESM2), *J. Adv. Model. Earth Syst.*, 12, e2019MS001916, <https://doi.org/10.1029/2019MS001916>,
1036 2020.
- 1037 de Baar, H. J. W., Boyd, P. W., Coale, K. H., Landry, M. R., Tsuda, A., Assmy, P., Bakker, D. C. E., Bozec, Y.,
1038 Barber, R. T., Brzezinski, M. A., Buesseler, K. O., Boye, M., Croot, P. L., Gervais, F., Gorbunov, M. Y., Harrison,
1039 P. J., Hiscock, W. T., Laan, P., Lancelot, C., Law, C. S., Lvasseur, M., Marchetti, A., Millero, F. J., Nishioka, J.,
1040 Nojiri, Y., van Oijen, T., Riebesell, U., Rijkenberg, M. J. A., Saito, H., Takeda, S., Timmermans, K. R., Veldhuis,
1041 M. J. W., Waite, A. M., and Wong, C.-S.: Synthesis of iron fertilization experiments: From the Iron Age in the
1042 Age of Enlightenment, *J. Geophys. Res.*, 110, C09S16, <https://doi.org/10.1029/2004JC002601>, 2005.
- 1043 de Baar, H., Gerringa, L., Laan, P., and Timmermans, K.: Efficiency of carbon removal per added iron in ocean
1044 iron fertilization, *Mar. Ecol. Prog. Ser.*, 364, 269–282, <https://doi.org/10.3354/meps07548>, 2008.
- 1045 Dohan, K. and Maximenko, N.: Monitoring ocean currents with satellite sensors, *Oceanography*, 23, 94–103,
1046 2010.
- 1047 Dutkiewicz, S., Ward, B. A., Monteiro, F., and Follows, M. J.: Interconnection between nitrogen fixers and iron
1048 in the Pacific Ocean: Theory and numerical model, *Global Biogeochem. Cy.*, 26, GB1012,
1049 <https://doi.org/10.1029/2011GB004039>, 2012.
- 1050 Elrod, V. A., Berelson, W. M., Coale, K. H., and Johnson, K. S.: The flux of iron from continental shelf sediments:
1051 A missing source for global budgets, *Geophys. Res. Lett.*, 31, L12307, <https://doi.org/10.1029/2004GL020216>,
1052 2004.
- 1053 Gamo, T., Okamura, K., Hatanaka, H., Hasumoto, H., Komatsu, D., Chinen, M., Mori, M., Tanaka, J., Hirota, A.
1054 and Tsunogai, U.: Hydrothermal plumes in the Gulf of Aden, as characterized by light transmission, Mn, Fe, CH₄
1055 and delta C-13-CH₄ anomalies, *Deep-Sea Res. Pt. II*, 121, 62–70, 2015.

- 1056 Garcia, H. E., Locarnini, R. A., Boyer, T. P., Antonov, J. I., Baranova, O. K., Zweng, M. M., Reagan, J. R., and
1057 Johnson, D. R.: World Ocean Atlas 2013, Volume 3: Dissolved Oxygen, Apparent Oxygen Utilization, and
1058 Oxygen Saturation, edited by: Levitus, S. and Mishonov, A., NOAA Atlas NESDIS, 75, 27 pp., 2014a.
- 1059 Garcia, H. E., Locarnini, R. A., Boyer, T. P., Antonov, J. I., Baranova, O. K., Zweng, M. M., Reagan, J. R., and
1060 Johnson, D. R.: World Ocean Atlas 2013, Volume 4: Dissolved Inorganic Nutrients (phosphate, nitrate, silicate),
1061 edited by: Levitus, S. and Mishonov, A., NOAA Atlas NESDIS, 76, 25 pp., 2014b.
- 1062 Garcia H. E., Boyer, T. P., Baranova, O. K., Locarnini, R. A., Mishonov, A. V., Grodsky, A., Paver, C. R.,
1063 Weathers, K. W., Smolyar, I. V., Reagan, J. R., Seidov, D., Zweng, M. M.: World Ocean Atlas 2018: Product
1064 Documentation, edited by: Mishonov, A., 2019.
- 1065 Geider, R. J. and La Roche, J.: The role of iron in phytoplankton photosynthesis, and the potential for iron-
1066 limitation of primary productivity in the sea, *Photosynth. Res.*, 39, 275–301, <https://doi.org/10.1007/bf00014588>,
1067 1994.
- 1068 Gent, P. R. and McWilliams, J. C.: Isopycnal mixing in ocean circulation models, *J. Phys. Oceanogr.*, 20, 150–
1069 155, [https://doi.org/10.1175/1520-0485\(1990\)020<0150:IMIOCM>2.0.CO;2](https://doi.org/10.1175/1520-0485(1990)020<0150:IMIOCM>2.0.CO;2), 1990.
- 1070 Grand, M. M., Measures, C. I., Hatta, M., Hiscock, W. T., Buck, C. S., and Landing, W. M.: Dust deposition in
1071 the eastern Indian Ocean: The ocean perspective from Antarctica to the Bay of Bengal, *Global Biogeochem.*
1072 *Cycles*, 29, 357–374, <https://doi.org/10.1002/2014gb004898>, 2015.
- 1073 Guieu, C., Al Azhar, M., Aumont, O., Mahowald, N., Lévy, M., Éthé, C., and Lachkar, Z.: Major impact of dust
1074 deposition on the productivity of the Arabian Sea, *Geophys. Res. Lett.*, 46, 6736–6744, 2019
- 1075 Gustafsson, O., Kruså, M., Zencak, Z., Sheesley, R. J., Granat, L., Engström, E., Praveen, P. S., Rao, P. S., Leck,
1076 C., and Rodhe, H.: Brown clouds over South Asia: biomass or fossil fuel combustion?, *Science*, 323, 495–498,
1077 <https://doi.org/10.1126/science.1164857>, 2009.
- 1078 Haake, B., Ittekkot, V., Rixen, T., Ramaswamy, V., Nair, R. R., and Curry, W. B.: Seasonality and interannual
1079 variability of particle fluxes to the deep Arabian Sea, *Deep-Sea Res. Pt. I*, 40, 1323–1344, 1993.
- 1080 Han, W., McCreary, J. P., Anderson, D. L. T., and Mariano, A. J.: Dynamics of the eastern surface jets in the
1081 equatorial Indian Ocean, *J. Phys. Oceanogr.*, 29, 2191–2209, [https://doi.org/10.1175/1520-
1082 0485\(1999\)029<2191:DOTESJ>2.0.CO;2](https://doi.org/10.1175/1520-0485(1999)029<2191:DOTESJ>2.0.CO;2), 1999.
- 1083 Harrison, C. S., Long, M. C., Lovenduski, N. S., and Moore, J. K.: Mesoscale Effects on Carbon Export: A Global
1084 Perspective, *Global Biogeochem. Cy.*, 32, 680–703, <https://doi.org/10.1002/2017GB005751>, 2018.
- 1085 Helly, J. J. and Levin, L. A.: Global distribution of naturally occurring marine hypoxia on continental margins,
1086 *Deep-Sea Res. Pt. I*, 51, 1159–1168, 2004.
- 1087 Holte, J., Talley, L. D., Gilson, J., and Roemmich, D.: An Argo mixed layer climatology and database, *Geophys.*
1088 *Res. Lett.*, 44, 5618–5626, <https://doi.org/10.1002/2017GL073426>, 2017.

1089 Huffman, G. J., Adler, R. F., Arkin, P., Chang, A., Ferraro, R., Gruber, A., Janowiak, J., McNab, A., Rudolf, B.,
1090 and Schneider, U.: The Global Precipitation Climatology Project (GPCP) Combined Precipitation Dataset, *B. Am.*
1091 *Meteorol. Soc.*, 78, 5–20, [https://doi.org/10.1175/1520-0477\(1997\)078<0005:TGPCPG>2.0.CO;2](https://doi.org/10.1175/1520-0477(1997)078<0005:TGPCPG>2.0.CO;2), 1997.

1092 Ilyina, T., Six, K. D., Segschneider, J., Maier-Reimer, E., Li, H., and Núñez-Riboni, I.: Global ocean
1093 biogeochemistry model HAMOCC: Model architecture and performance as component of the MPI-Earth system
1094 model in different CMIP5 experimental realizations, *J. Adv. Model. Earth Sy.*, 5, 287–315,
1095 <https://doi.org/10.1029/2012MS000178>, 2013.

1096 Jickells, T. D., An, Z. S., Andersen, K. K., Baker, A. R., Bergametti, G., Brooks, N., Cao, J. J., Boyd, P. W., Duce,
1097 R. A., Hunter, K. A., Kawahata, H., Kubilay, N., laRoche, J., Liss, P. S., Mahowald, N., Prospero, J. M., Ridgwell,
1098 A. J., Tegen, I., and Torres, R.: Global Iron Connections between Desert Dust, Ocean Biogeochemistry, and
1099 *Climate, Science*, 308, 67–71, 2005.

1100 Jin, Q., Wei, J., Pu, B., Yang, Z. L., and Parajuli, S. P.: High summertime aerosol loadings over the Arabian Sea
1101 and their transport pathways, *J. Geophys. Res.-Atmos.*, 123, 10568–10590,
1102 <https://doi.org/10.1029/2018jd028588>, 2018.

1103 Johnson, K. S., Chavez, F. P., and Friederich, G. E.: Continental-shelf sediment as a primary source of iron for
1104 coastal phytoplankton, *Nature*, 398, 697–700, <https://doi.org/10.1038/19511>, 1999.

1105 Kalnay, E., Kanamitsu, M., Kistler, R., Collins, W., Deaven, D., Gandin, L., Iredell, M., Saha, S., White, G.,
1106 Woollen, J., Zhu, Y., Leetmaa, A., Reynolds, R., Chelliah, M., Ebisuzaki, W., Higgins, W., Janowiak, J., Mo, K.
1107 C., Ropelewski, C., Wang, J., Jenne, R., and Joseph, D.: The NCEP/NCAR 40-Year Reanalysis Project, *B. Am.*
1108 *Meteorol. Soc.*, 77, 437–471, [https://doi.org/10.1175/1520-0477\(1996\)077<0437:TNYRP>2.0.CO;2](https://doi.org/10.1175/1520-0477(1996)077<0437:TNYRP>2.0.CO;2), 1996.

1109 Kawamiya, M. and Oschlies, A.: Formation of a basin-scale surface chlorophyll pattern by Rossby waves,
1110 *Geophys. Res. Lett.*, 28, 4139–4142, 2001.

1111 Kohfeld, K. E. and Harrison, S. P.: DIRTMAP: the geological record of dust, *Earth-Science Rev.*, 54, 81–114,
1112 [https://doi.org/10.1016/S0012-8252\(01\)00042-3](https://doi.org/10.1016/S0012-8252(01)00042-3), 2001.

1113 Kok, J. F., Adebisi, A. A., Albani, S., Balkanski, Y., Checa-Garcia, R., Chin, M., Colarco, P. R., Hamilton, D. S.,
1114 Huang, Y., Ito, A., Klose, M., Li, L., Mahowald, N. M., Miller, R. L., Obiso, V., Pérez García-Pando, C., Rocha-
1115 Lima, A., and Wan, J. S.: Contribution of the world's main dust source regions to the global cycle of desert dust,
1116 *Atmos. Chem. Phys.*, 21, 8169–8193, <https://doi.org/10.5194/acp-21-8169-2021>, 2021.

1117 Końe, V., Aumont, O., Lévy, M., and Resplandy, L.: Physical and Biogeochemical Controls of the Phytoplankton
1118 Seasonal Cycle in the Indian Ocean: A Modeling Study, *Geoph. Monog. Series*, 185, 147–166,
1119 <https://doi.org/10.1029/2008GM000700>, 2009.

1120 Kumar, A., Suresh, K., and Rahaman, W.: Geochemical Characterization of Modern Aeolian Dust over the
1121 Northeastern Arabian Sea: Implication for Dust Transport in the Arabian Sea, *Science of the Total Environment*,
1122 729, 138576, <https://doi.org/10.1016/j.scitotenv.2020.138576>, 2020.

- 1123 Kuttippurath, J., Sunanda, N., Martin, M. V., and Chakraborty, K.: Tropical storms trigger phytoplankton blooms
1124 in the deserts of north Indian Ocean, *NPJ Climate and Atmospheric Science*, 4, 11,
1125 <https://doi.org/10.1038/s41612-021-00166-x>, 2021.
- 1126 Large, W. G., McWilliams, J. C., and Doney, S. C.: Oceanic vertical mixing: A review and a model with a
1127 nonlocal boundary layer parameterization, *Rev. Geophys.*, 32, 363–403, 1994.
- 1128 Large, W. G. and Yeager, S. G.: The global climatology of an interannually varying air-sea flux data set, *Clim.*
1129 *Dynam.*, 33, 341–364, <https://doi.org/10.1007/s00382-008-0441-3>, 2009.
- 1130 Léon, J. F. and Legrand, M.: Mineral dust sources in the surroundings of the North Indian Ocean, *Geophys. Res.*
1131 *Lett.*, 30, 1309, <https://doi.org/10.1029/2002GL016690>, 2003.
- 1132 Letelier, R. M., Karl, D. M., Abbott, M. R., and Bidigare, R. R.: Light driven seasonal patterns of chlorophyll and
1133 nitrate in the lower euphotic zone of the North Pacific Subtropical Gyre, *Limnol. Oceanogr.*, 49, 508–519,
1134 <https://doi.org/10.4319/lo.2004.49.2.0508>, 2004.
- 1135 Levitus, S., T. Boyer, M. Concright, D. Johnson, T. O'Brien, J. Antonov, C. Stephens, and R. Garfield:
1136 Introduction, Vol. I, World Ocean Database 1998, NOAA Atlas NESDIS 18, 346 pp, 1998.
- 1137 Lévy, M., Shankar, D., André, J., Shenoi, S., Durand, F., and de Boyer Montégut, C.: Basin-wide seasonal
1138 evolution of the Indian Ocean's phytoplankton blooms, *J. Geophys. Res.-Oceans*, 112, C12014,
1139 <https://doi.org/10.1029/2007JC004090>, 2007.
- 1140 Liu, J. P., Xue, Z., Ross, K., Wang, H. J., Yang, Z. S., and Gao, S.: Fate of sediments delivered to the sea by Asian
1141 large rivers: Long-distance transport and formation of remote alongshore clinothems, *The Sedimentary Record*,
1142 7(4), 4–9, <https://doi.org/10.2110/sedred.2009.4.4>, 2009.
- 1143 Liu, X., Ma, P.-L., Wang, H., Tilmes, S., Singh, B., Easter, R. C., Ghan, S. J., and Rasch, P. J.: Description and
1144 evaluation of a new four-mode version of the Modal Aerosol Module (MAM4) within version 5.3 of the
1145 Community Atmosphere Model, *Geosci. Model Dev.*, 9, 505–522, <https://doi.org/10.5194/gmd-9-505-2016>,
1146 2016.
- 1147 Long, M. C., Moore, J. K., Lindsay, K., Levy, M. N., Doney, S. C., Luo, J. Y., Krumhardt, K. M., Letscher, R.
1148 T., Grover, M., and Sylvester, Z. T.: Simulations with the Marine Biogeochemistry Library (MARBL), *J. Adv.*
1149 *Model. Earth Syst.*, accepted, <https://doi.org/10.1029/2021MS002647>, 2021.
- 1150 Madhu, N., Jyothibabu, R., Maheswaran, P., Gerson, V. J., Gopalakrishnan, T., and Nair, K.: Lack of seasonality
1151 in phytoplankton standing stock (chlorophyll a) and production in the western Bay of Bengal, *Cont. Shelf Res.*,
1152 26, 1868–1883, 2006.
- 1153 Madhupratap, M., Prasanna Kumar, S., Bhattathiri, P. M. A., DileepKumar, M., Raghukumar, S., Nair, K. K. C.,
1154 and Ramaiah, N.: Mechanism of the biological response to winter cooling in the northeastern Arabian Sea, *Nature*,
1155 384, 549–552, 1996.
- 1156 Madhupratap, M., Gauns, M., Ramaiah, N., Kumar, S. P., Muraleedharan, P., de Sousa, S., Sardessai, S., and
1157 Muraleedharan, U.: Biogeochemistry of the Bay of Bengal: physical, chemical and primary productivity

- 1158 characteristics of the central and western Bay of Bengal during summer monsoon 2001, *Deep-Sea Res. Pt. II*, 50,
1159 881–896, [https://doi.org/10.1016/S0967-0645\(02\)00611-2](https://doi.org/10.1016/S0967-0645(02)00611-2), 2003.
- 1160 Mahowald, N. M., Engelstaedter, S., Luo, C., Sealy, A., Artaxo, P., Benitez-Nelson, C., Bonnet, S., Chen, Y.,
1161 Chuang, P. Y., Cohen, D. D., Dulac, F., Herut, B., Johansen, A. M., Kubilay, N., Losno, R., Maenhaut, W., Paytan,
1162 A., Prospero, J. M., Shank, L. M., and Siefert, R. L.: Atmospheric iron deposition: global distribution, variability,
1163 and human perturbations, *Ann. Rev. Mar. Sci.*, 1, 245–278,
1164 <https://doi.org/10.1146/annurev.marine.010908.163727>, 2009.
- 1165 Masumoto, Y. and Meyers, G.: Forced Rossby waves in the southern tropical Indian Ocean, *J. Geophys. Res.-*
1166 *Oceans*, 103, 27589–27602, <https://doi.org/10.1029/98JC02546>, 1998.
- 1167 Mayorga, E., Seitzinger, S. P., Harrison, J. A., Dumont, E., Beusen, A. H. W., Bouwman, A. F., Fekete, B. M.,
1168 Kroeze, C. and van Drecht, G.: Global Nutrient Export from WaterSheds 2 (NEWS 2): Model development and
1169 implementation, *Environ. Modell. Softw.*, 25, 837–853, <https://doi.org/10.1016/j.envsoft.2010.01.007>, 2010.
- 1170 McLennan, S. M.: Relationships between the trace element composition of sedimentary rocks and upper
1171 continental crust, *Geochemistry, Geophysics, Geosystems*, 2(4), 1021, <http://doi.org/10.1029/2000gc000109>,
1172 2001.
- 1173 McPhaden, M. J., Wang, Y., and Ravichandran, M.: Volume transports of the Wyrki jets and their relationship
1174 to the Indian Ocean dipole, *J. Geophys. Res.-Oceans*, 120, 5302–5317, 2015.
- 1175 Measures, C. I. and Vink, S.: Seasonal variations in the distribution of Fe and Al in the surface waters of the
1176 Arabian Sea, *Deep-Sea Res. Pt. II*, 46, 1597–1622, 1999.
- 1177 Mills, M. M., Ridame, C., Davey, M., La Roche, J., and Geider, R. J.: Iron and phosphorus co-limit nitrogen
1178 fixation in the eastern tropical North Atlantic, *Nature*, 429, 292, <https://doi.org/10.1038/nature02550>, 2004.
- 1179 Moffett, J. W., Goepfert, T. J., and Naqvi, S. W. A.: Reduced iron associated with secondary nitrite maxima in
1180 the Arabian Sea, *Deep-Sea Res. Pt. I*, 54, 1341–1349, <https://doi.org/10.1016/j.dsr.2007.04.004>, 2007.
- 1181 Moffett, J. W., Vedamati, J., Goepfert, T. J., Pratihary, A., Gauns, M., and Naqvi, S. W. A.: Biogeochemistry of
1182 iron in the Arabian Sea, *Limnol. Oceanogr.*, 60, 1671–1688, <https://doi.org/10.1002/lno.10132>, 2015.
- 1183 Moore, J. K., Doney, S. C., and Lindsay, K.: Upper ocean ecosystem dynamics and iron cycling in a global three-
1184 dimensional model, *Global Biogeochem. Cy.*, 18, GB4028, <https://doi.org/10.1029/2004GB002220>, 2004.
- 1185 Moore, J. K. and Braucher, O.: Sedimentary and mineral dust sources of dissolved iron to the world ocean,
1186 *Biogeosciences*, 5, 631–656, <https://doi.org/10.5194/bg-5-631-2008>, 2008.
- 1187 Moore, C. M., Mills, M. M., Achterberg, E. P., Geider, R. J., La Roche, J., Lucas, M. I., McDonagh, E. I., Pan,
1188 X., Poulton, A. J., and Rijkenberg, M. J.: Large-scale distribution of Atlantic nitrogen fixation controlled by iron
1189 availability, *Nat. Geosci.*, 2, 867–871, 2009.

- 1190 Moore, C. M., Mills, M. M., Arrigo, K. R., Berman-Frank, I., Bopp, L., Boyd, P. W., Galbraith, E. D., Geider,
1191 R. J., Guieu, C., Jaccard, S. L., Jickells, T. D., Roche, J. L., Lenton, T. M., Mahowald, N. M., Marañón, E.,
1192 Marinov, I., Moore, J. K., Nakatsuka, T., Oschlies, A., Saito, M. A., Thingstad, T. F., Tsuda, A., and Ulloa, O.:
1193 Processes and patterns of oceanic nutrient limitation, *Nat. Geosci.*, 6, 701–710,
1194 <https://doi.org/10.1038/NGEO1765>, 2013a.
- 1195 Moore, J. K., Lindsay, K., Doney, S. C., Long, M. C., and Misumi, K.: Marine Ecosystem Dynamics and
1196 Biogeochemical Cycling in the Community Earth System Model CESM1(BGC): Comparison of the 1990s with
1197 the 2090s under the RCP4.5 and RCP8.5 Scenarios, *J. Climate*, 26, 9291–9312, <https://doi.org/10.1175/jcli-d-12->
1198 00566.1, 2013b.
- 1199 Moorthy, K. K. and Babu, S. S.: Aerosol black carbon over Bay of Bengal observed from an island location, Port
1200 Blair: Temporal features and long-range transport, *J. Geophys. Res.*, 111, D17205, doi:10.1029/2005JD006855,
1201 2006.
- 1202 Morrison, J. M., Codispoti, L. A., Smith, S. L., Wishner, K., Flagge, C., Gardner, W. D., Gaurin, S., Naqvi, S.,
1203 Manghnani, V., Prosperie, L., and Gundersen, J. S.: The oxygen minimum zone in the Arabian Sea during 1995,
1204 *Deep-Sea Res. Pt. II*, 46, 1903–1931, 1999.
- 1205 Morrison, J. M., Codispoti, L. A., Gaurin, S., Jones, B., Manghanani, V., and Zheng, Z.: Seasonal variations of
1206 hydrographic and nutrient fields during the US JGOFS Arabian Sea Process Study, *Deep-Sea Res. Pt. II*, 45,
1207 2053–2101, 1998.
- 1208 Naqvi, S. W. A., Moffett, J. W., Gauns, M. U., Narvekar, P. V., Pratihary, A. K., Naik, H., Shenoy, D. M.,
1209 Jayakumar, D. A., Goepfert, T. J., Patra, P. K., Al-Azri, A., and Ahmed, S. I.: The Arabian Sea as a high-nutrient,
1210 low-chlorophyll region during the late Southwest Monsoon, *Biogeosciences*, 7, 2091–2100,
1211 <https://doi.org/10.5194/bg-7-2091-2010>, 2010.
- 1212 Nishioka, J., Obata, H., and Tsumune, D.: Evidence of an extensive spread of hydrothermal dissolved iron in the
1213 Indian Ocean, *Earth Planet. Sci. Lett.*, 361, 26–33, <https://doi.org/10.1016/j.epsl.2012.11.040>, 2013.
- 1214 Olsen, A., Key, R. M., van Heuven, S., Lauvset, S. K., Velo, A., Lin, X., Schirnick, C., Kozyr, A., Tanhua, T.,
1215 Hoppema, M., Jutterström, S., Steinfeldt, R., Jeansson, E., Ishii, M., Pérez, F. F., and Suzuki, T.: The Global
1216 Ocean Data Analysis Project version 2 (GLODAPv2) – an internally consistent data product for the world ocean,
1217 *Earth Syst. Sci. Data*, 8, 297–323, <https://doi.org/10.5194/essd-8-297-2016>, 2016.
- 1218 Pérégaud, C., and Delecluse, P.: Annual sea level variations in the southern tropical Indian Ocean from Geosat
1219 and shallow water simulations, *J. Geophys. Res.*, 97, 20169–20178, <https://doi.org/10.1029/92JC01961>, 1992.
- 1220 Pham, A. L. D., and Ito, T.: Anthropogenic iron deposition alters the ecosystem and carbon balance of the Indian
1221 Ocean over a centennial timescale, *J. Geophys. Res.-Oceans*, 126, e2020JC016475,
1222 <https://doi.org/10.1029/2020JC016475>, 2021.

- 1223 Pollard, R. T., Salter, I., Sanders, R. J., Lucas, M. I., Moore, C. M., Mills, R. A., Statham, P. J., Allen, J. T., Baker,
1224 A. R., Bakker, D. C. E., Charette, M. A., Fielding, S., Fones, G. R., French, M., Hickman, A. E., Holland, R. J.,
1225 Hughes, J. A., Jickells, T. D., Lampitt, R. S., Morris, P. J., Nedelec, F. H., Nielsdottir, M., Planquette, H., Popova,
1226 E. E., Poulton, A. J., Read, J. F., Seeyave, S., Smith, T., Stinchcombe, M., Taylor, S., Thomalla, S., Venables, H.
1227 J., Williamson, R., and Zubkov, M. V.: Southern Ocean deep-water carbon export enhanced by natural iron
1228 fertilization, *Nature*, 457, 577–580, <https://doi.org/10.1038/nature07716>, 2009.
- 1229 Prasanna Kumar, S., Madhupratap, M., Dileep Kumar, M., Muraleedharan, P. M., de Souza, S. N., Gauns, M.,
1230 and Sarma, V. V. S. S.: High biological productivity in the central Arabian Sea during summer monsoon driven
1231 by Ekman pumping and lateral advection, *Curr. Sci.*, 81, 1633–1638, 2001.
- 1232 Prasanna Kumar, S., Nuncio, M., Narvekar, J., Kumar, A., Sardesai, S., de Souza, S. N., Gauns, M., Ramaiah, N.,
1233 and Madhupratap, M.: Are eddies nature's trigger to enhance biological productivity in the Bay of Bengal?,
1234 *Geophys. Res. Lett.*, 31, L07309, <https://doi.org/10.1029/2003GL019274>, 2004.
- 1235 Prasanna Kumar, S., Divya David, T., Byju, P., Narvekar, J., Yoneyama, K., Nakatani, N., Ishida, A., Horii, T.,
1236 Masumoto, Y., and Mizuno, K.: Bio-physical coupling and ocean dynamics in the central equatorial Indian Ocean
1237 during 2006 Indian Ocean Dipole, *Geophys. Res. Lett.*, 39, L14601, doi:10.1029/2012GL052609, 2012.
- 1238 Ramaswamy, V. and Gaye, B.: Regional variations in the fluxes of foraminifera carbonate, coccolithophorid
1239 carbonate and biogenic opal in the northern Indian Ocean, *Deep-Sea Res. Pt. I*, 53, 271–293,
1240 doi:10.1016/j.dsr.2005.11.003, 2006.
- 1241 Ramaswamy, V., Gaye, B., Shirodkar, P. V., Rao, P. S., Chivas, A. R., Wheeler, D., and Thwin, S.: Distribution
1242 and sources of organic carbon, nitrogen and their isotopic signatures in sediments from the Ayeyarwady
1243 (Irrawaddy) continental shelf, northern Andaman Sea, *Marine Chem.*, 111(3), 137–150.
1244 <https://doi.org/10.1016/j.marchem.2008.04.006>, 2008.
- 1245 Raven, J. A.: The iron and molybdenum use efficiencies of plant growth with different energy, carbon and nitrogen
1246 sources, *New Phytol.*, 109, 279–287, <https://doi.org/10.1111/j.1469-8137.1988.tb04196.x>, 1988.
- 1247 Redi, M. H.: Oceanic isopycnal mixing by coordinate rotation, *J. Phys. Oceanogr.*, 12, 1154–1158,
1248 [https://doi.org/10.1175/1520-0485\(1982\)012<1154:OIMBCR>2.0.CO;2](https://doi.org/10.1175/1520-0485(1982)012<1154:OIMBCR>2.0.CO;2), 1982.
- 1249 Resplandy, L., Lévy, M., Madec, G., Pous, S., Aumont, O., and Kumar, D.: Contribution of mesoscale processes
1250 to nutrient budgets in the Arabian Sea, *J. Geophys. Res.*, 116, C11007, <https://doi.org/10.1029/2011JC007006>,
1251 2011.
- 1252 Rixen, T., Gaye, B., and Emeis, K.-C.: The monsoon, carbon fluxes, and the organic carbon pump in the northern
1253 Indian Ocean, *Prog. Oceanogr.*, 175, 24–39, <https://doi.org/10.1016/j.pocean.2019.03.001>, 2019.

- 1254 Robinson, R. A. J., Bird, M. I., Oo, N. W., Hoey, T. B., Aye, M. M., Higgitt, D. L., Lud, X. X., Swe, A., Tun, T.,
1255 and Win, S. L.: The Irrawaddy river sediment flux to the Indian Ocean: the original nineteenth-century data
1256 revisited, *J. Geol.*, 115, 629–640, <https://doi.org/10.1086/521607>, 2007.
- 1257 Sander, S. and Koschinsky, A.: Metal flux from hydrothermal vents increased by organic complexation, *Nat.*
1258 *Geosci.*, 4, 145–150, <https://doi.org/10.1038/ngeo1088>, 2011.
- 1259 Sathyendranath, S., Brewin, R. J., Brockmann, C., Brotas, V., Calton, B., Chuprin, A., Cipollini, P., Couto, A. B.,
1260 Dingle, J., Doerffer, R., Donlon, C., Dowell, M., Farman, A., Grant, M., Groom, S., Horseman, A., Jackson, T.,
1261 Krasemann, H., Lavender, S., Martinez-Vicente, V., Mazeran, C., Mélin, F., Moore, T. S., Müller, D., Regner, P.,
1262 Roy, S., Steele, C. J., Steinmetz, F., Swinton, J., Taberner, M., Thompson, A., Valente, A., Zühlke, M.,
1263 Brando, V. E., Feng, H., Feldman, G., Franz, B. A., Frouin, R., Gould, R. W., Hooker, S. B., Kahru, M.,
1264 Kratzer, S., Mitchell, B. G., Muller-Karger, F. E., Sosik, H. M., Voss, K. J., Werdell, J., and Platt, T.: An Ocean-
1265 Colour Time Series for Use in Climate Studies: The Experience of the Ocean-Colour Climate Change Initiative
1266 (OC-CCI), *Sensors*, 19, 4285, <https://doi.org/10.3390/s19194285>, 2019.
- 1267 Schlitzer, R., Masferrer Dodas, E., Adjou, M., Anderson, R. F., Andre, F., Cockwell, D. M., et al.: The
1268 GEOTRACES Intermediate Data Product 2021 (IDP2021), NERC EDS British Oceanographic Data Centre NOC,
1269 doi: 10.5285/cf2d9ba9-d51d-3b7c-e053-8486abc0f5fd, 2021.
- 1270 Schlosser, C., Klar, J. K., Wake, B. D., Snow, J. T., Honey, D. J., Woodward, E. M. S., Lohan, M. C., Achterberg,
1271 E. P., and Moore, C. M.: Seasonal ITCZ migration dynamically controls the location of the (sub)tropical Atlantic
1272 biogeochemical divide, *P. Natl. Acad. Sci. USA*, 111, 1438–1442, 2014.
- 1273 Schmidtko, S., Stramma, L., and Visbeck, M.: Decline in global oceanic oxygen content during the past five
1274 decades, *Nature*, 542, 335–339, <https://doi.org/10.1038/nature21399>, 2017.
- 1275 Schott, F. and McCreary, J. P.: The monsoon circulation of the Indian Ocean, *Prog. Oceanogr.*, 51, 1–123,
1276 [https://doi.org/10.1016/S0079-6611\(01\)00083-0](https://doi.org/10.1016/S0079-6611(01)00083-0), 2001.
- 1277 Sedwick, P. N. and DiTullio, G. R.: Regulation of algal blooms in Antarctic shelf waters by the release of iron
1278 from melting sea ice, *Geophys. Res. Lett.*, 24, 2515–2518, <https://doi.org/10.1029/97GL02596>, 1997.
- 1279 Singh, N. D., Chinni, V., and Singh, S. K.: Dissolved aluminium cycling in the northern, equatorial and subtropical
1280 gyre region of the Indian Ocean, *Geochim. Cosmochim. Ac.*, 268, 160–185, doi: 10.1016/j.gca.2019.09.028, 2020.
- 1281 Sholkovitz, E. R., Sedwick, P. N., Church, T. M., Baker, A. R., and Powell, C. F.: Fractional solubility of aerosol
1282 iron: Synthesis of a global-scale data set, *Geochim. Cosmochim. Ac.*, 89, 173–189,
1283 <https://doi.org/10.1016/j.gca.2012.04.022>, 2012.
- 1284 Smith, R., Jones, P., Briegleb, B., Bryan, F., Danabasoglu, G., Dennis, J., Dukowicz, J., Eden, C., Fox-Kemper,
1285 B., Gent, P., Hecht, M., Jayne, S., Jochum, M., Large, W., Lindsay, K., Maltrud, M., Norton, N., Peacock, S.,

- 1286 Vertenstein, M., and Yeager, S.: The Parallel Ocean Program (POP) reference manual, Ocean component of the
1287 Community Climate System Model (CCSM), LANL Tech. Report, LAUR-10-01853, 141 pp., 2010.
- 1288 Smith, S. L.: Understanding the Arabian Sea: Reflections on the 1994-1996 Arabian Sea Expedition, *Deep-Sea*
1289 *Res. Pt. II*, 48, 1385–1402, 2001.
- 1290 Srinivas, B., Sarin, M. M., and Kumar, A.: Impact of anthropogenic sources on aerosol iron solubility over the
1291 Bay of Bengal and the Arabian Sea, *Biogeochemistry*, 110, 257–268, [https://doi.org/10.1007/s10533-011-9680-](https://doi.org/10.1007/s10533-011-9680-1)
1292 1, 2012.
- 1293 Srinivas, B. and Sarin, M. M.: Atmospheric dry-deposition of mineral dust and anthropogenic trace metals to the
1294 Bay of Bengal, *J. Mar. Syst.*, 126, 56–68, <https://doi.org/10.1016/j.jmarsys.2012.11.004>, 2013.
- 1295 Strutton, P. G., Coles, V. J., Hood, R. R., Matear, R. J., McPhaden, M. J., and Phillips, H. E.: Biogeochemical
1296 variability in the central equatorial Indian Ocean during the monsoon transition, *Biogeosciences*, 12, 2367–2382,
1297 <https://doi.org/10.5194/bg-12-2367-2015>, 2015.
- 1298 Sunda, W. G. and Huntsman, S. A.: Iron uptake and growth limitation in oceanic and coastal phytoplankton, *Mar.*
1299 *Chem.*, 50, 189–206, [https://doi.org/10.1016/0304-4203\(95\)00035-P](https://doi.org/10.1016/0304-4203(95)00035-P), 1995.
- 1300 Tagliabue, A., Bopp, L., Dutay, J.-C., Bowie, A. R., Chever, F., Jean-Baptiste, P., Bucciarelli, E., Lannuzel, D.,
1301 Remenyi, T., Sarthou, G., Aumont, O., Gehlen, M., and Jeandel, C.: Hydrothermal contribution to the oceanic
1302 dissolved iron inventory, *Nat. Geosci.*, 3, 252–256, <https://doi.org/10.1038/ngeo818>, 2010.
- 1303 Tagliabue, A., Mtshali, T., Aumont, O., Bowie, A. R., Klunder, M. B., Roychoudhury, A. N., and Swart, S.: A
1304 global compilation of dissolved iron measurements: focus on distributions and processes in the Southern Ocean,
1305 *Biogeosciences*, 9, 2333–2349, <https://doi.org/10.5194/bg-9-2333-2012>, 2012.
- 1306 Tagliabue, A., Aumont, O., and Bopp, L.: The impact of different external sources of iron on the global carbon
1307 cycle, *Geophys. Res. Lett.*, 41, 920–926, <https://doi.org/10.1002/2013GL059059>, 2014.
- 1308 Tagliabue, A., Aumont, O., De'Ath, R., Dunne, J. P., Dutkiewicz, S., Galbraith, E., Misumi, K., Moore, J. K.,
1309 Ridgwell, A., Sherman, E., Stock, C., Vichi, M., Völker, C., and Yool, A.: How well do global ocean
1310 biogeochemistry models simulate dissolved iron distributions?, *Global Biogeochem. Cy.*, 30, 2,
1311 <https://doi.org/10.1002/2015GB005289>, 2016.
- 1312 Takeda, S., Kamarani, A., and Kawanobe, K.: Effects of nitrogen and iron enrichments on phytoplankton
1313 communities, *Mar. Chem.*, 50, 229–241, [https://doi.org/10.1016/0304-4203\(95\)00038-S](https://doi.org/10.1016/0304-4203(95)00038-S), 1995.
- 1314 Thushara, V., Vinayachandran, P. N. M., Matthews, A. J., Webber, B. G. M., and Queste, B. Y.: Vertical
1315 distribution of chlorophyll in dynamically distinct regions of the southern Bay of Bengal, *Biogeosciences*, 16,
1316 1447–1468, <https://doi.org/10.5194/bg-16-1447-2019>, 2019.
- 1317 Twining, B. S., Rauschenberg, S., Morton, P. L., and Vogt, S.: Metal contents of phytoplankton and labile
1318 particulate material in the North Atlantic Ocean, *Progr. Oceanogr.*, 137, 261–283,
1319 <https://doi.org/10.1016/j.pocan.2015.07.001>, 2015.

- 1320 Twining, B. S., Rauschenberg, S., Baer, S. E., Lomas, M. W., Martiny, A. C., and Antipova, O. M.: A nutrient
1321 limitation mosaic in the eastern tropical Indian Ocean, *Deep-Sea Res. Pt. II*, 166, 125–140,
1322 <https://doi.org/10.1016/j.dsr2.2019.05.001>, 2019.
- 1323 Twining, B. S., Antipova, O., Chappell, P. D., Cohen, N. R., Jacquot, J. E., Mann, E. L., et al.: Taxonomic and
1324 nutrient controls on phytoplankton iron quotas in the ocean, *Limnology and Oceanography Letters*, 6(2), 96–106,
1325 <https://doi.org/10.1002/lol2.10179>, 2021.
- 1326 Unger, D., Ittekkot, V., Schäfer, P., Tiemann, J., and Reschke, S.: Seasonality and interannual variability of
1327 particle fluxes to the deep Bay of Bengal: influence of riverine input and oceanographic processes, *Deep-Sea Res.*
1328 *Pt. II*, 50, 897–923, 2003.
- 1329 Vialard, J., Duvel, J. P., McPhaden, M. J., Bouruet-Aubertot, P., Ward, B., Key, E., Bourras, D., Weller, R.,
1330 Minnett, P., Weill, A., Cassou, C., Eymard, L., Fristedt, T., Basdevant, C., Dandonneau, Y., Duteil, O., Izumo,
1331 T., de Boyer Montégut, C., Masson, S., and Kennan, S.: Cirene: Air – Sea Interactions in the Seychelles – Chagos
1332 Thermocline Ridge Region, *B. Am. Meteor. Soc.*, 90, 45–62, <https://doi.org/10.1175/2008BAMS2499.1>, 2009.
- 1333 Vidya, P. J. and Prasanna Kumar, S.: Role of mesoscale eddies on the variability of biogenic flux in the northern
1334 and central Bay of Bengal, *J. Geophys. Res.-Oceans*, 118, 5760–5771, <https://doi.org/10.1002/jgrc.20423>, 2013.
- 1335 Vidya, P. J., Prasanna Kumar, S., Gauns, M., Verenkar, A., Unger, D., and Ramaswamy, V.: Influence of physical
1336 and biological processes on the seasonal cycle of biogenic flux in the equatorial Indian Ocean, *Biogeosciences*,
1337 10, 7493–7507, <https://doi.org/10.5194/bg-10-7493-2013>, 2013.
- 1338 Vinayachandran, P. N., Chauhan, P., Mohan, M., and Nayak, S.: Biological response of the sea around Sri Lanka
1339 to summer monsoon, *Geophys. Res. Lett.*, 31, L0I302, <https://doi.org/10.1029/2003GL018533>, 2004.
- 1340 Vinayachandran, P. N., Shankar, D., Vernekar, S., Sandeep, K. K., Amol, P., Neema, C. P., and Chatterjee, A.: A
1341 summer monsoon pump to keep the Bay of Bengal salty, *Geophys. Res. Lett.*, 40, 1777–1782,
1342 <https://doi.org/10.1002/grl.50274>, 2013.
- 1343 Vu, H. and Sohrin, Y.: Diverse stoichiometry of dissolved trace metals in the Indian Ocean, *Sci. Rep.*, 3,
1344 [doi:10.1038/srep01745](https://doi.org/10.1038/srep01745), 2013.
- 1345 Wang, S., Bailey, D., Lindsay, K., Moore, J. K., and Holland, M.: Impact of sea ice on the marine iron cycle and
1346 phytoplankton productivity, *Biogeosciences*, 11, 4713–4731, <https://doi.org/10.5194/bg-11-4713-2014>, 2014.
- 1347 Webber, B. G. M., Matthews, A. J., Vinayachandran, P. N., Neema, C. P., Sanchez-Franks, A., Vijith, V., Amol,
1348 P., and Baranowski, D. B.: The dynamics of the Southwest Monsoon current in 2016 from high-resolution in situ
1349 observations and models, *J. Phys. Oceanogr.*, 48, 2259–2282, <https://doi.org/10.1175/JPO-D-17-0215.1>, 2018.
- 1350 Wiggert, J. D., and Murtugudde, R. G.: The sensitivity of the Southwest Monsoon phytoplankton bloom to
1351 variations in aeolian iron deposition over the Arabian Sea, *J. Geophys. Res.*, 112, C05005,
1352 <https://doi.org/10.1029/2006JC003514>, 2007.

- 1353 Wyrski, K.: An equatorial jet in the Indian Ocean, *Science*, 181, 262–264,
1354 <https://doi.org/10.1126/science.181.4096.262>, 1973.
- 1355 Xie, P. and Arkin, P. A.: Global precipitation: A 17-year monthly analysis based on gauge observations, satellite
1356 estimates, and numerical model outputs, *B. Am. Meteorol. Soc.*, 78, 2539–2558, [https://doi.org/10.1145/1520-0477\(1997\)078<2539:GPAYAMA>2.0.CO;2](https://doi.org/10.1145/1520-0477(1997)078<2539:GPAYAMA>2.0.CO;2), 1997.
- 1358 Yang, X., Zhao, C., Yang, Y., and Fan, H.: Long-term multi-source data analysis about the characteristics of
1359 aerosol optical properties and types over Australia, *Atmos. Chem. Phys.*, 21, 3803–3825,
1360 <https://doi.org/10.5194/acp-21-3803-2021>, 2021.
- 1361 Yoon, J.-E., Yoo, K.-C., Macdonald, A. M., Yoon, H.-I., Park, K.- T., Yang, E. J., Kim, H.-C., Lee, J. I., Lee, M.
1362 K., Jung, J., Park, J., Lee, J., Kim, S., Kim, S.-S., Kim, K., and Kim, I.-N.: Reviews and syntheses: Ocean iron
1363 fertilization experiments – past, present, and future looking to a future Korean Iron Fertilization Experiment in
1364 the Southern Ocean (KIFES) project, *Biogeosciences*, 15, 5847–5889, <https://doi.org/10.5194/bg-15-5847-2018>,
1365 2018.
- 1366 Zhang, Y., Rossow, W. B., Lacis, A. A., Oinas, V., and Mishchenko, M. I.: Calculation of radiative fluxes from
1367 the surface to top of atmosphere based on ISCCP and other global data sets: Refinements of the radiative transfer
1368 model and the input data, *J. Geophys. Res.*, 109, D19105, <https://doi.org/10.1029/2003JD004457>, 2004.
- 1369